ETH Institute for Particle Physics

ETHZ-IPP Internal Report 2006-02
March 2006

DIPLOMA THESIS

Test of a high temperature superconductor coil in liquid nitrogen and liquid argon

Thomas Strauss
under the supervision of
Prof. Dr. André Rubbia

ETH Zürich, Switzerland

HUMBOLDT-UNIVERSITÄT ZU BERLIN

Test of a high temperature superconductor coil in liquid nitrogen and liquid argon

Diplomarbeit

Humboldt-Universität zu Berlin
Mathematisch-Naturwissenschaftliche Fakultät I
Institut für Physik

eingereicht von

Thomas Strauss
geb. am 15.03.1981 in Berlin

1. Gutachter: Prof. Dr. Thomas Lohse (HU-Berlin, BRD)
2. Gutachter: Prof. Dr. André Rubbia (ETH Zürich, Schweiz)

Berlin, März 2006

Abstract

For an application with a magnetized liquid argon time projection chamber ('LAr TPC'), a high temperature superconductor ('HTS') wire was tested. The resistivity of the HTS wire for different magnetic fields perpendicular and parallel to the wire was measured in LAr (T_{LAr}=87 K) and LN_2 (T_{LN_2}=77 K). A small solenoid consisting of four so called 'pancake coils' was built and successfully tested. The produced magnetic field was up to 0.2 T in LN_2 and 0.1 T in LAr. With a HTS solenoid consisting of 47 pancake coils the B-field could be increased to about 0.25 T.

Zusammenfassung

Für die Anwendungsmöglichkeit einer magnetisierten Flüssigargon Zeitprojektionskammer ('liquid argon time projection chamber', 'LAr TPC') wurde ein Hochtemperatursupraleiter Draht ('HTS wire') getestet. Der Widerstand des Drahtes wurde für verschiedene parallele und senkrechte Feldkomponenten in Flüssigargon (T_{LAr}=87 K) und Flüssigstickstoff (T_{LN_2}=77) gemessen. Ein kleiner Solenoid aus vier sogenannten Scheibenspulen ('pancakes') wurde gebaut und erfolgreich getestet. Das erreichte Magnetfeld betrug 0.2 T im flüssigen Stickstoff und 0.1 T im flüssigen Argon. Mit einer HTS-Spule, bestehend aus 47 Scheibenspulen, könnte ein Magnetfeld von 0.25 T erzeugt werden.

You can know the name of a bird in all the languages of the world, but when you're finished, you'll know absolutely nothing whatever about the bird... So let's look at the bird and see what it's doing – that's what counts.

Richard Feynman (1918 - 1988)

Contents

1 Introduction

1.1 Motivation

During the last years, the ICARUS collaboration (Imaging Cosmic And Rare Underground Signal) [1] has developed the liquid argon time projection chamber (LAr TPC) technique. The ICARUS experiment is one of the two long baseline (732 km) neutrino experiments that are placed in the CERN Neutrinos to Gran Sasso beam (CNGS) [2]. The ICARUS experiment is a 600 ton LAr TPC supposed to detect τ decays of the 20 GeV ν_μ-neutrino beam as well as solar and atmospheric neutrinos. It allows nucleon decay search as well. From 1977, when Carlo Rubbia proposed the liquid argon time projection chamber (LAr TPC) [3] to now a lot of R&D work has been done, influencing the detector layout and increasing the knowledge in the fields of argon purification, wire chambers and electronics as well as the data acquisition. Starting from small prototypes, a 600 ton detector was built and tested and is now installed at the Gran Sasso laboratory (LNGS) in Italy [4] (see Figure 1).

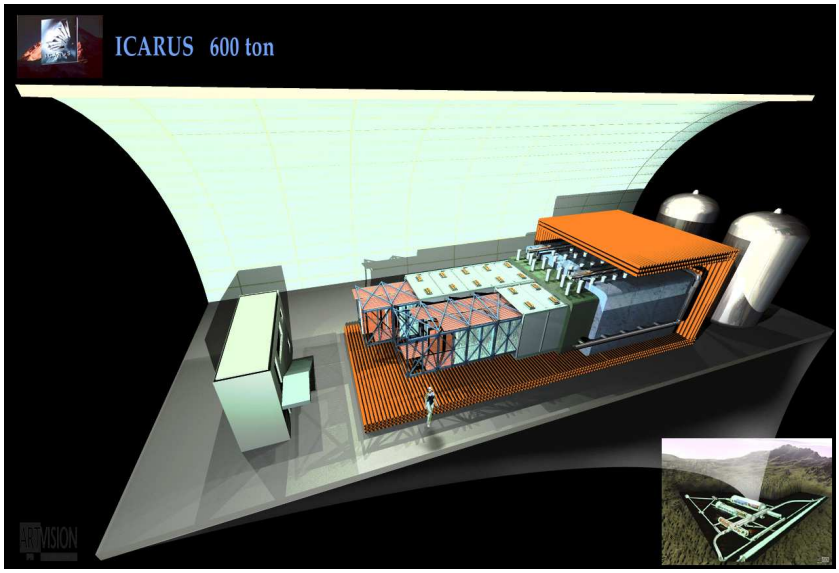

Figure 1: *The ICARUS 600 ton detector at the Hall B of the LNGS. Picture from LNGS website.*

1.1.1 The LAr TPC

The LAr TPC is a special form of a time projection chamber, in which instead of the normally gaseous drift medium liquid argon is used [5]. Using liquid argon as filling medium for the detector allows the TPC not only to be a 3-dimensional homogeneous tracking device with high resolution imaging properties, but also to work as a fine grain calorimeter for stopping particles due to the measurement of

the energy loss dE/dx along the charged particle tracks. Scintillation light and Cherenkov light can be observed as well by photomultipliers as the liquid argon is transparent and the emitted photons have not enough energy to excite the argon atoms. By measuring the time the ionization electrons need to reach the anode wires a high spatial resolution of 0.5 mm is reached in the drift direction (sampling time 400 ns). To achieve this spatial resolution the electron drift velocity has to be well known and also a simple relation for tracks with different angles has to exist. Therefore, the chambers are designed in a way that the shape and homogeneity of the electric field is adjusted carefully with layers of field-shaping electrodes enclosing the detector volume in which the electrons are drifting orthogonal to the read-out wire planes. For the reconstruction of particle tracks projected to the chamber planes multiple (i.e. three) read-out planes with different wire orientations are used (see Figure 2).

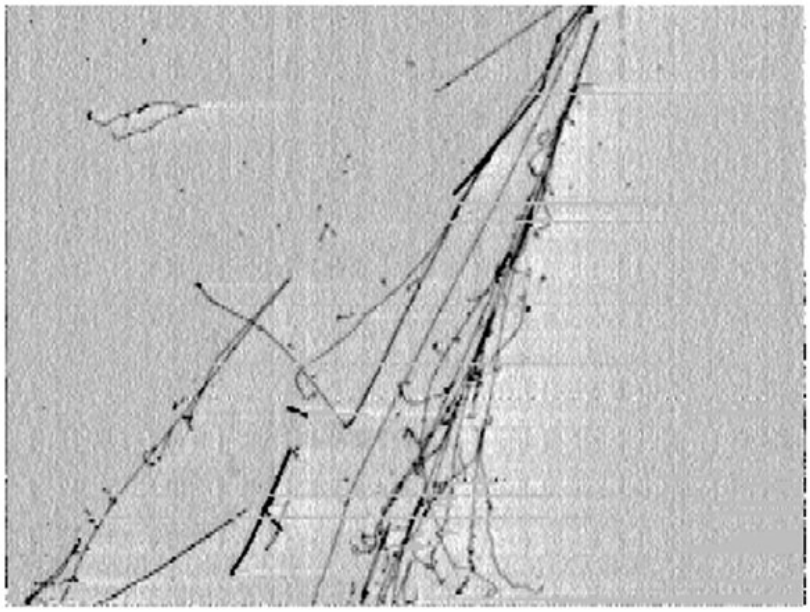

Figure 2: *Cosmic ray shower observed in the ICARUS 3-ton prototype at CERN. Photon conversion into pairs as well as pion and muon decays are clearly visible in the electromagnetic showers. Picture from ICARUS collaboration web site.*

The first planes are set to potentials such that the first two planes are transparent for drifting electrons (induction planes). The electrons are collected at the third plane (collection plane). At the induction planes the induced signal from the electrons passing through the plane is measured. A three dimensional track reconstruction is possible when looking for signals having the same drift time in the read-out data of the wire planes.

The typical expected charge for a minimum ionizing particle (mip) is of the order of 13 000 electrons for 2 mm track length drifting with a velocity of 1.6 mm/μs for a

drift field of 0.5 kV/cm [6]. Combined with the long drift paths in detectors with big sensitive volumes (for ICARUS 1.5 m drift distance) the electrons spend a long time in liquid argon, therefore the concentration of electronegative impurities (especially oxygen) in LAr has to be minimized to avoid the capturing of the drifting electrons by electronegative atoms or molecules, thus, decreasing the charge arriving at the sensor planes. Therefore, a highly purified drift volume and ultra-pure LAr with a contamination of less than 0.1 ppb (O_2 equivalent) is needed. As a consequence of the short free mean path length of electrons in liquid argon no charge multiplication occurs in LAr, since the drifting electrons do not gain enough kinetic energy between their collisions with atoms to ionize them. Thus, the wire read out is difficult, but a direct measurement of the ionization charge is possible when a low noise preamplifier is used. This makes a LAr TPC an ideal realtime detector for the field of neutrino physics and to study nucleon decays [7] with the ICARUS experiment, but other possibilities exist. For further details see several articles written by the ICARUS collaboration [1, 8, 9].

1.1.2 Other experimental techniques

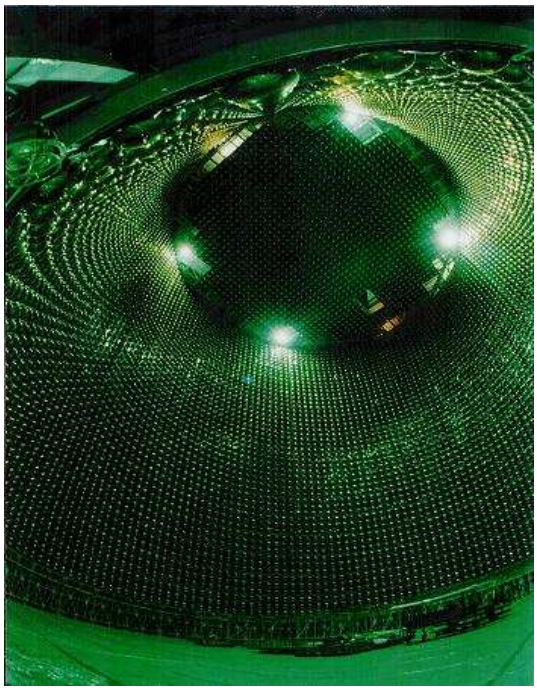

Figure 3: *The SUPERKAMIOKANDE detector, wall and top with about 9000 photomultiplier tubes which are used to measure the Cherenkov light of crossing neutrinos. Picture from the SUPERKAMIOKANDE collaboration web site.*

The energy of the charged decay particles is either measured via Cherenkov radiation [10] (in the AMANDA [11], ICE CUBE [12], ANTARES [13], KAMIOKANDE

and SUPERKAMIOKANDE [14] experiment with photo multipliers or via a scintillator liquid like in the CHOOZ experiment [15]) or via a combination of several tracker methods like in the OPERA experiment [16].

Counting the neutrino reactions can also be done with radiochemical experiments like Homestake [17] (see Figure 8), measuring the total ν_e-flux over a long time via the inverse beta decay reaction of gallium or chloride, e.g. ${}^{71}Ga + \nu_e \rightarrow {}^{72}Ge + e^-$. Extracting the radioactive daughter atoms from the detector volume and measuring their decay allows the precise measurement of the total number of events.

1.1.3 Future experimental plans

All realtime detectors have their experimental advantages and disadvantages. Cherenkov light detectors (CLD) are easily scalable to high masses, but require a good light detection efficiency and background suppression while the LAr TPC allows complete track reconstruction and has a lower energy threshold for detected particles and detects multiple showers better than a CLD [23]. Disadvantages are the cooling of the argon below 89 K and the constraint that the argon has to be ultrapure to reach long drift paths. Like mentioned before, the LAr TPC can act as a calorimeter for particles stopping inside the drift volume. Unfortunately no charge discrimination was possible so far neither with the CLD nor with the LAr TPC. For future neutrino experiments three different types of neutrino beams are considered to be used:

- super beams, e.g. pion beams of high intensity
- beta beams, e.g. radioactive storage rings
- or neutrino factories, e.g. muon storage rings

While detectors for super and beta beams do not need a magnetic field, detectors for neutrino factories have to measure the sign of the leading lepton to study CP-violation in the lepton sector, i.e. they have to be magnetized.

1.1.4 The LAr TPC in a magnetic field

Applying a magnetic field to the LAr TPC brings a great improvement to the LAr TPC technique, since it provides new experimental possibilities like charge discrimination, momentum measurement of escaping particles (e.g. high energy muons) and very precise kinematics, only limited by multiple scattering [18, 19, 20, 21, 22]. A LAr TPC with a mass scale of 30 kton up to 100 kton be a perfectly suited detector for a neutrino factory, and also deliver a rich physics program in solar and astrophysical neutrino physics and the search for a leptonic CP violation as well. R&D work is still going on to improve the imaging properties of the LAr TPC technique [23, 24, 25, 26, 27, 28, 29]. A first test with a small magnetized LAr TPC was done

at the ETH Zürich using a conventional solenoid [6]. The following lines are quoted (shortened) from this thesis:

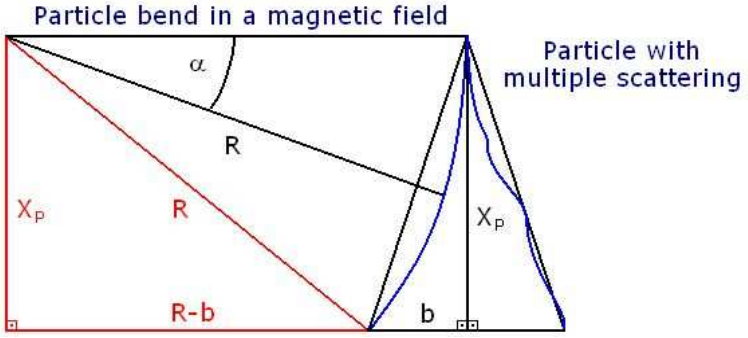

Figure 4: *Definition of the bending parameter b of a particle, where X_P is the thickness of the particle trajectory projected into the bending plane, and R is the bending radius. Picture from [6].*

If the orientation of the magnetic field is chosen in a way that the bending direction is in the direction of the drift the best spatial resolution is achieved since the Lorentz angle is small. The magnetic field needed for charge discrimination for a thickness x in LAr (x_p is the projected thickness into the bending plane) is given by the bending parameter b [20], defined in Figure 4. For small bending angles $\alpha \ll 1$ it can be approximated by $b \approx \frac{x_p^2}{2R} = \frac{0.3\,B[Tesla](x([m])^2\,\cos\lambda}{2p[GeV]}$. The multiple scattering contributes to b and can be estimated as $MS \approx \frac{0.02\,(x[m])^{3/2}}{p[GeV]}$ [30]. The requirement for a 3σ charge discrimination can be written as $2b > 3$ MS, which implies a field strength of $B \geq \frac{0.2\,[Tesla]}{\sqrt{x[m]}\,\cos\lambda}$. For long penetrating tracks like muons, a field of 0.1 T allows to discriminate the charge for tracks longer than 4 m. This corresponds to a muon momentum threshold of 800 MeV/c. The early showering of electrons makes their charge identification difficult, so the track-length usable for charge discrimination is limited to a few radiation lengths. In practice, charge discrimination is possible for

- $x = 1X_0 \rightarrow B > 0.5$ *Tesla,*
- $x = 2X_0 \rightarrow B > 0.4$ *Tesla or*
- $x = 3X_0 \rightarrow B > 0.3$ *Tesla.*

Simulations showed that the determination of the charge of electrons of energy in the range between 1 and 5 GeV is feasible with good purity, provided the field has a strength in the range of 1 T. Preliminary estimates showed that these electrons exhibit an average curvature sufficient to have electron charge discrimination with an efficiency of 20 % for a contamination with the wrong charge of less than 1 % [21]. The momentum resolution of a particle bending in a uniform magnetic field can be found when using the curvature, defined as $k \equiv 1/R$, with $\frac{\Delta p_t}{p_t} = \Delta k\,\frac{p_t}{0.3\,B}$. At

low momenta, one can safely neglect the contribution from the position measurement error given the readout pitch and drift time resolution and the momentum resolution is then given by $\frac{\Delta p_t}{p_t} \approx \frac{0.14}{B[Tesla]\sqrt{L[m]}\,\cos\lambda}$ *where L is the trajectory length in space. In the presence of a magnetic field a Lorentz force is acting on each moving charge, modifying the drift properties of the electrons. As a consequence, the electrons will not move along the electric field lines, but on a straight line at an angle* α *to the E-field. It can be seen that for the case of perpendicular E- and B-fields the Lorentz angle* α *is given by* $\tan\alpha = 2\mu B$*, where* μ *is the electron mobility. The Lorentz angle is expected to be very small in the liquid, e.g.* 1.7° *for E = 500 V/cm and B=0.5 T. Embedding the volume of argon into a magnetic field should therefore not alter the imaging properties of the detector and the measurement of the bending of charged hadrons or penetrating muons would allow a precise determination of the momentum and a determination of their charge.*

For the thesis of M. Laffranchi a conventional copper solenoid with water cooling was used, producing a magnetic field up to 0.55 T. For a massive detector in the kiloton range a conventional magnet would dissipate 17 MW of heating power at a field of 0.2 T (or 88 MW for 1 T). Due to this heat production strong constraint on the thermal insulation of the liquid argon volume arise. Since the liquid argon has a temperature of about 89 K at a pressure of 1.2 bar, the use of an high temperature superconductor (HTS) was considered to build the solenoid for large mass scale detectors [25, 31]. The use of a superconductor not only minimizes the requirements of the insulation, but also the current could flow in absence of a power supply due to the zero-resistivity of a superconductor. The feasibility of applying a HTS solenoid to a LAr TPC is investigated in this diploma thesis.

1.2 Brief overview over the history of neutrino physics [32]

1.2.1 The beta decay problem and the "birth" of the neutrino

In the year 1896 Henry Becquerel discovered a new kind of radiation coming from uranium salts [33]. In 1899 Rutherford showed that two different kinds of radiation existed. He called them alpha and beta radiation [34]. In 1902 beta radiation was tagged as electron-beams by Pierre and Maria Curie [35]. Since in beta radiation only one particle was emitted, it should have a fixed energy. But different studies showed a continuous spectrum (by Meitner, Hahn, Wilson and Chadwick). This was a real problem for the physicists of that time, since energy and angular momentum conversation seemed to be violated. On the fourth of December 1930 Wolfgang Pauli wrote a letter to some colleagues at a workshop in Tübingen, announcing the possibility of *electrically neutral particles, ...to call neutrons, which have spin 1/2.* He expected the neutron mass to be *of the same order of magnitude as the electron mass and in any event not larger than 0.01 proton masses. The continuous beta spectrum would then become understandable by the assumption that in beta decay a neutron is emitted in addition to the electron such that the sum of the energies of*

the neutron and the electron is constant.... In February 1932, a new particle was observed by Chadwick [36], calling it neutron, but this particle was surely different to the type of neutron Pauli suggested. Thus, in 1933 Pauli again stressed that his particles, now called neutrinos to distinguish them from the heavier neutrons, have only a mass in the range of electrons or even zero [37]. In the year 1933 Perrin [38] showed that the neutrino mass has to be much smaller than the electron mass and Joliot-Curie [39] observed the beta plus decay. The first anti-particle, the positron, was observed by Anderson [40] in 1932, which was verifying the Dirac theory, which was predicting the existence of particle and antiparticles [41].

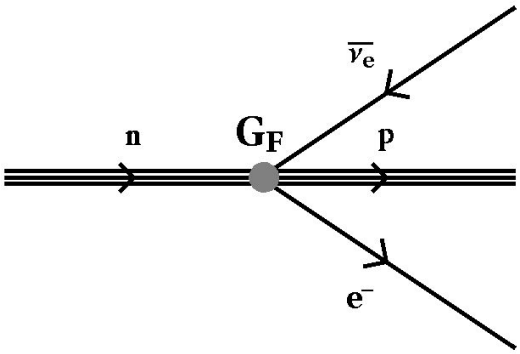

Figure 5: *Tree Feynman diagram of the 4 fermia point interaction. Picture from the Wikipedia web site.*

Fermi built a theory of the beta decay as a 4 fermion point interaction including the neutrino [42] analog to the electro-magnetic interaction (see Figure 5). The theory of the four fermion vector current $H_{weak} \sim j^{\mu_{hadron}} j_{\mu_{lepton}}$ with $j^\mu = V^\mu$ was changed into a V-A current ($j^\mu = V^\mu - A^\mu$) when parity violation was observed. The theory was not renormalizable, but worked fine as a phenomenological description for low energies. A renormalizable theory was presented in 1974 (see paragraph 'How many lepton families exist?').

Shortly afterwards, in 1934, Bethe and Peierls calculated the cross section (interaction probability) between neutrinos and matter to be $\sigma \sim 10^{-44}$ cm^2 at $E_\nu = 1\,\mathrm{MeV}$ [43]. This is several billion times smaller than the one of the electron with matter and corresponds for lead to a mean free path length of one light year, i.e., neutrinos were known to be very difficult to detect.

1.2.2 The first observed neutrino.

The small cross section allows the observation only with large and heavy, but extremely sensitive detectors, and although physicists continued their research on the beta decay, no direct observation of a neutrino was possible. The discovery of the nuclear chain reaction gave the physicists an intense neutrino source and in 1946

Pontecorvo suggested to use the resulting neutrino flux to observe the inverse beta decay [44].

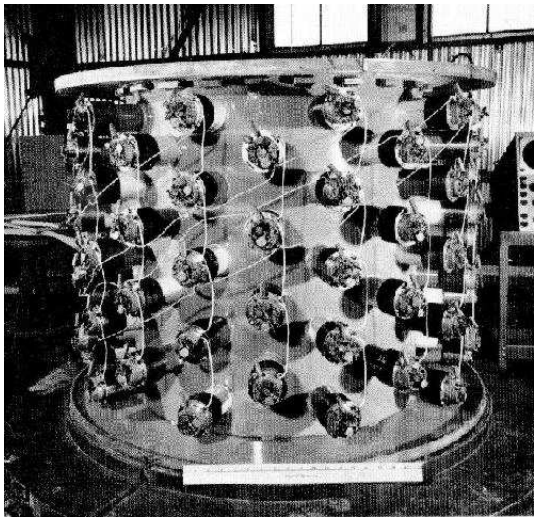

Figure 6: *Detector of the 1953 inverse beta decay experiment by Reines and Cowan. Picture from [32].*

In 1953 Cowan and Reines proposed an experimental setup using a nuclear reactor as neutrino source (Hanford nuclear plant, Washington) [45]. As detector a target made out of a mixture of 400 liters of a water and cadmium chloride was used and the measurements were finished in 1953, but no convincing results were achieved [46]. In 1956 the experiment was repeated at the Savannah River nuclear plant, South Carolina, and due to a careful preparation (especially by reducing the background) the neutrino was discovered with the reaction $\overline{\nu}_e + p \rightarrow n + e^+$ [47], by observing delayed gamma's from n-capture and e^+ e_- annihilation.

1.2.3 Are there different neutrino-types?

After the discovery of the neutrino the question occurred, whether a difference between the neutrino emitted in beta decay and the neutrino observed in cosmic-rays exists. In 1959 Schwartz proposed an intense neutrino beam using the pion decay, the pions were produced by a few GeV proton beam hitting a target [48]. The cooperation of Schwartz, Ledermann, Steinberger and Gaillard, inspired by Cronin's spark chamber in Princeton [49], developed the detector for the experiment and the cross section was calculated by Lee and Yang, announcing that if the reaction $n + \nu \rightarrow e^- + p$ is not observed, two different neutrino types had to exist [50]. In 1962 the construction of a 10 ton spark chamber filled with neon gas and shielded from muons with an iron layer was finished at the Brookhaven accelerator and the measurement started. Several millions of neutrinos per hour were delivered by the accelerator, and 40 events were recorded. While for 6 events the final interaction

particle was identified as electron, the other final particles were muons. That was the evidence of two neutrino types, since else the ratio should have been equal to one [51].

1.2.4 How many lepton families exists?

After the discovery of an electron- and a muon-neutrino, other experiments in the sixties and seventies brought information in the field of the weak interaction of neutrinos. Especially the CERN experiments CHARM I & 2, CDHS and BEBC showed that the nucleon consists of point-like scattering centers, the quarks. When in 1970 Glashow, Iliopoulos and Maiani proposed the existence of a second quark family [52], their hypothesis was experimentally confirmed in 1974. In 1973 neutral currents were observed with the bubble chamber Gargamelle [53].

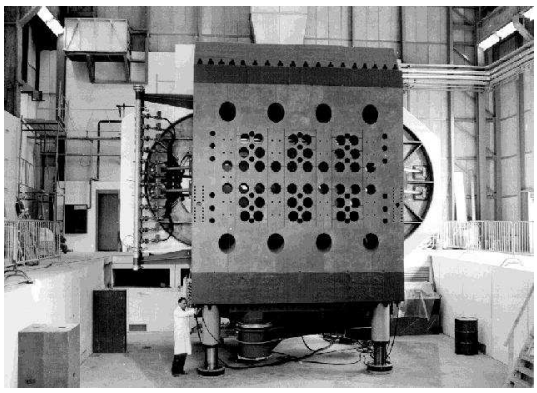

Figure 7: *Bubble chamber Gargamelle at CERN, which allowed the observation of neutral currents. Picture from [32].*

In a neutral current interaction the neutrino is not transformed into an electron or muon. 1974 Salam [54], Glashow [55] and Weinberg [56] unified the two theories of weak and electromagnetic interactions into an electro-weak theory: a boson (photon) transports the electromagnetic interaction and the weak interaction is transported with either a W^+, a W^- or the Z-Boson. The beta decay was now explained as a neutron transforming into a proton by emitting a W^-, which shortly afterwards decayed into an e^- and $\overline{\nu}_e$. In the Standard Model of elementary particles, the ν's are considered to be massless.

When in 1977 the Lederman group at the Stanford accelerator observed the b-quark, the first member of a third quark family was found. The τ-lepton was found by Perl [57] around the same time, thus, also a third lepton family was supposed to exist. Finally, in 1983 the W-Boson was observed in the UA1 experiment and shortly afterwards the Z-Boson. This closed the circle and finally, nearly 90 years after the first observation of the beta decay, a consistent theory for the beta decay was confirmed. Finally, in 1989 lifetime measurements of the Z-boson showed that

only three light neutrinos could exist, but still neither the missing t-quark nor the missing τ-neutrino were observed. In fact, the experimentally observation of the t-quark had to wait until 1994 [58] while the ν_τ was not observed before the year 2000, when it was found at the Fermilab [59].

1.2.5 Do neutrinos have a (small) mass?

The Homestake mine detector of Davis, based on chloride and running since 1969, catching some solar neutrinos per year gave the astonishing result that above a neutrino energy of 1MeV the neutrino flux predicted by the standard solar model is about three times bigger than observed with the detector [17]; this is the so-called solar neutrino deficit. The detector was only sensitive to electron-neutrinos.

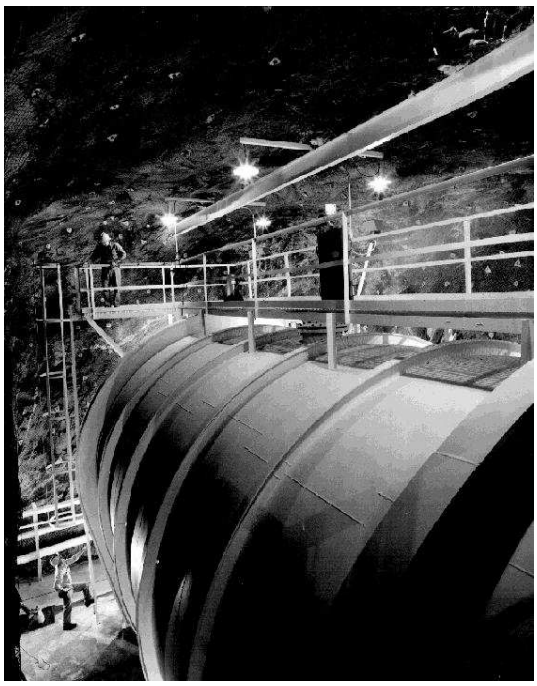

Figure 8: *Homestake mine detector, based on chloride, detects neutrinos via the inverse beta decay. Picture from [32].*

The most plausible explanation was that the neutrinos had oscillated on their way to the earth. A non-zero neutrino mass could lead to the quantum-mechanically possibility of neutrino oscillation [60].

Different neutrinos masses m_i (i=1,2,3) lead to mass eigenstates ν_i which can be a mixture of the flavour or interaction eigenstates $\nu_{e,\mu,\tau}$. Like for the CKM mixing-matrix in the quark sector, the flavour eigenstates can be expressed in terms of the

mass eigenstates with an unitary mixing matrix U, the MNSP[1]-matrix.

$$\begin{pmatrix} \nu_e \\ \nu_e \\ \nu_e \end{pmatrix} = \begin{pmatrix} 1 & 0 & 0 \\ 0 & c_{23} & s_{23} \\ 0 & -s_{23} & c_{23} \end{pmatrix} \begin{pmatrix} c_{13} & 0 & s_{13}e^{i\delta} \\ 0 & 1 & 0 \\ -s_{13}e^{i\delta} & 0 & c_{13} \end{pmatrix} \begin{pmatrix} c_{12} & s_{12} & 0 \\ -s_{12} & c_{12} & 0 \\ 0 & 0 & 1 \end{pmatrix} \quad (1)$$

This matrix, where $c_{ij} \equiv \cos(\theta_{ij})$ and $s_{ij} \equiv \sin(\theta_{ij})$, contains 3 mixing angles θ_{ij} ($0 \leq \theta_{ij} \leq \pi/2$), the possibility of CP violation is expressed with the phase δ ($0 \leq \delta \leq 2\pi$); for CP conservation δ equals zero. The oscillation amplitudes depend on the mixing angles and the oscillation lengths (for a given neutrino energy) on the differences of the squared masses $\Delta m^2_{ij} = m^2_i - m^2_j$, details of the mathematical formalism are explained in literature [61]. There are only two independent Δm^2_{ij}, the difference of the squared masses $\Delta m^2_{21} = m^2_2 - m^2_1$ and $\Delta m^2_{32} = m^2_3 - m^2_2$ (the third mass difference $\Delta m^2_{31} = m^2_3 - m^2_1$ is equal to $\Delta m^2_{32} + \Delta m^2_{21}$).

Solar and atmospheric neutrino measurements suggest a strong mass hierarchy, i.e., $\Delta m^2_{21} = \Delta m^2_{solar} \ll \Delta m^2_{31} \approx \Delta m^2_{32} = \Delta m^2_{atmosphere}$, and the CHOOZ reactor experiment limits θ_{13} to small values [15]. In this case the observed neutrino oscillations can be described by the simpler two-neutrino-mixing. E.g., the solar neutrino $\nu_e \rightarrow \nu_\mu$ oscillation can approximately be written as:

$$P(\nu_e \rightarrow \nu_\mu) = \sin^2\left(\frac{\Delta m^2_{solar} L}{4E_\nu}\right) \cdot \sin^2(2\theta_{solar}) \quad (2)$$

where L is the flight path and θ_{solar} is the mixing angle θ_{12}.

In 1985 Mikheyev and Smirnov enhanced the Wolfenstein theory on neutrino oscillation with a resonance effect which can occur when neutrinos travel through matter, the MSW effect [62]: even if in vacuum the mixing angle is small, it can became large for certain ν-energies and electron densities. Hence, the solar neutrino deficit may be caused by the oscillation of neutrinos on their path through the sun.

1.2.6 Neutrino oscillation experiments

Several experiments tried to observe the oscillation effect on earth, leading in 1984 to two reactor experiments (Goesgen and Bugey) putting limits on the neutrino oscillation (if the mass difference between ν_μ and ν_e was more than 0.1 eV, then the mixing has to be less than 10%).

Other experiments like GALLEX [63] and SAGE [64], inverse beta decay experiments based on gallium, or KAMIOKANDE [14] a water cerenkov light detector, originally intended as detector for proton decays, were set up to confirm that deficit. In 1995 the GALLEX and SAGE experiment confirmed a discrepancy of 40% between the theoretical predicted and the observed solar neutrino spectrum. The KAMIOKANDE experiment observed even a deficit of 50% for solar neutrinos with

[1]Maki, Nakagawa, Sakata, Pontecorvo

an energy of more than 7.5 MeV. These differences in the deficit can be explained by the MSW theory. In 1996 the Los Alamos LSND experiment observed 22 $\overline{\nu}_e$-events when only four were expected from π^+ and μ^+ decays [65]. The only reasonable explanation was an oscillation of $\overline{\nu}_\mu \rightarrow \overline{\nu}_e$, but the parameters gave a controversial result that does not fit in the picture, thus, the experiment is planned to be repeated at Fermilab. In 1998 the NOMAD and CHORUS experiments searching for ν_τ neutrinos in the ν_μ beam of the CERN SPS accelerator delivered the result of no neutrino oscillation for $sin^2(2\theta_m) > 4.2 \cdot 10^{-3}$ or $\Delta m^2 > 1$ eV^2.

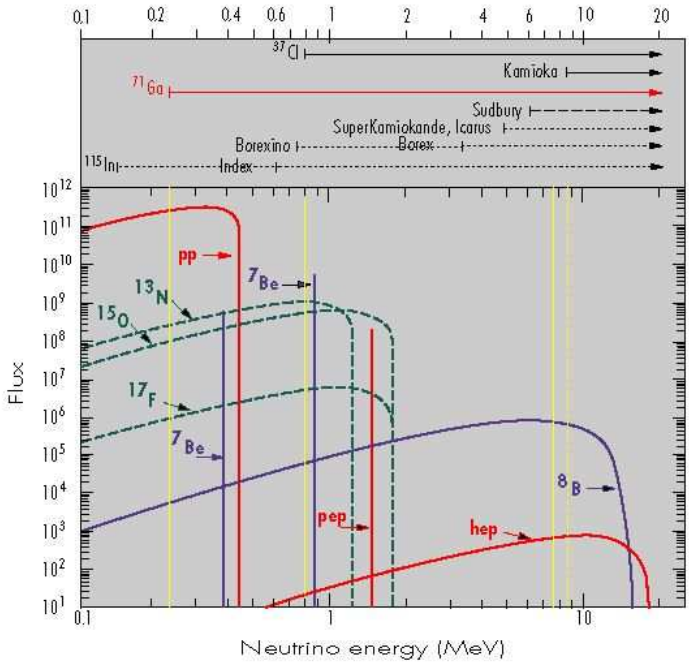

Figure 9: *Predicted solar neutrino flux depending on the neutrino energy, the energy domains to which different experiments are sensitive are shown above the plot. Picture from [32].*

In 1998 the SUPERKAMIOKANDE experiment observed a deficit of the atmospheric ν_μ when they compared the number of the neutrinos going up through the whole earth with the number of neutrinos coming from top, i.e. from the earth's atmosphere. The analysis was not that clear, but a refined analysis in the year 2004 brought the final proof of the atmospheric oscillation effect [14], confirmed by the K2K experiment [66]. Another experiment confirming the solar neutrino oscillation effect was the SNO experiment, sensitive to ν_e in CC and to all neutrinos in NC interactions [67]. Though the total predicted flux of the standard solar model was confirmed, the number of electron neutrinos was less than expected. Resulting from measurements of the tritium beta decay in Mainz the today upper mass limit for ν_e is 2.3 eV [68].

1.2.7 The current status [6]

Summarizing the results from the experiments, parameters of the MNSP- and the 2 neutrino mixing scheme can be determined.

2-neutrino mixing parameters:

-Solar neutrinos

For the two neutrino mixing scheme of solar neutrinos the best fit the SAGE, GALLEX, SNO, KamLAND [69] and SUPERKAMIOKANDE experiment is:

$$\sin^2\theta_{solar} = 0.29$$
$$\Delta m^2_{solar} = 6.0 \times 10^{-5} eV^2$$

-Atmospheric neutrinos

For the two neutrino mixing scheme of atmospheric neutrinos the best fit to the SUPERKAMIOKANDE, Soudan-2 [70] and MARCO [71] experiments with a 3σ range is:

$$\sin^2\theta_{atmosphere} = 0.5 \qquad 0.3 \leq \sin^2\theta_{atmosphere} \leq 0.7$$
$$\Delta m^2_{atmosphere} = 2.5 \times 10^{-3} eV^2 \qquad 1.2 \times 10^{-3} eV^2 \leq \Delta m^2_{atmosphere} \leq 4.8 \times 10^{-3} eV^2$$

3-neutrino mixing parameters:

For the 3-neutrino mixing parameters all data from the mentioned experiments as well as the results from Palo Verde [72] the best fit with a 3σ range is:

$$\sin^2\theta_{12} = 0.3 \qquad 0.23 \leq \sin^2\theta_{12} \leq 0.39$$
$$\sin^2\theta_{23} = 0.52 \qquad 0.36 \leq \sin^2\theta_{23} \leq 0.67$$
$$\Delta m^2_{21} = 6.9 \times 10^{-5} eV^2 \qquad 5.4 \times 10^{-5} eV^2 \leq \Delta m^2_{21} \leq 9.5 \times 10^{-5} eV^2$$
$$\Delta m^2_{31} = 2.6 \times 10^{-3} eV^2 \qquad 1.4 \times 10^{-3} eV^2 \leq \Delta m^2_{31} \leq 3.7 \times 10^{-3} eV^2$$

For the value of θ_{13} only an upper limit, mainly given by the CHOOZ experiment, exists:

$$\theta_{13} \begin{cases} 0.070 & (0.12) & (solar + KamLAND) \\ 0.028 & (0.066) & (CHOOZ + atmospheric) \\ 0.029 & (0.054) & (globaldata) \end{cases}$$

1.2.8 What is coming next?

The Hamiltonian of the GSW-theory, named after Glashow, Salam and Weinberg, does not include mass terms for the neutrinos [55, 54, 56]. The experimental results show that the neutrino masses are many orders below the mass of the corresponding

leptons, so that their mass can be ignored for most calculations. However, from the observation of neutrino oscillations it is clear that the Standard Model has to be extended, to account for neutrino mixing. The today commonly known extensions are grand unified theories (GUT) predicting massive neutrinos or theories of super-symmetry (SUSY, SUSY-GUT). These theories partly allow predictions of the neutrino mass and mixing parameters.

New experiments like KATRIN [73], CNGS [2] and T2K [74] should bring further knowledge in the field of physics beyond the standard model. If neutrinos have a mass (and oscillations indicate that) also right-handed neutrinos are theoretically possible, i.e. not forbidden, but since only the left-handed neutrinos can interact with the electro-weak force, the right-handed neutrinos would just interact with gravitation. This could solve the dark matter problem and there are several experiments ongoing to search for these so called Weakly Interacting Massive Particles (WIMPs) [75].

1.3 Superconductivity

1.3.1 History

[76] In 1911 the physicist K. Onnes [77] from the Leiden University observed the effect of superconductivity when he cooled mercury below the transition temperature of 4 K and the resistance of the mercury suddenly disappeared. In 1933 W. Meissner and R. Ochsenfeld [78] discovered that superconductive material repels magnetic fields, today known as 'Meissner effect'.

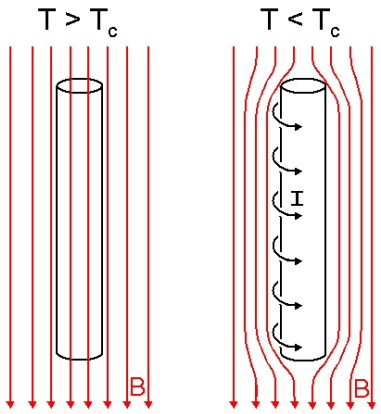

Figure 10: *Meissner effect, expulsion of magnetic flux in a superconductor below a critical field H_c. Picture from the world wide web.*

Since 1911 many other superconductive metals, alloys and compounds were found, reaching a transition temperature up to 17.5 K. In 1962 the first commercial used wire made out of niobium and titanium was produced. At that time the first copper-clad niobium-titan electromagnets for particle-accelerators were produced by Rutherford-Appleton Laboratory [79], and in 1987 the first superconductive accelerator, the Tevatron started operation at Fermilab [80] in the USA.

The first phenomenological theory to describe superconductivity was developed by L.D. Landau and V.L. Ginzburg [81] in 1950 as a macroscopic theory, describing the properties of superconductors thermodynamically as second order phase transition using a parameter Ψ to describe the depth of the superconductive phase (for Ψ equals zero the system is in normal conducting state). By minimizing the free energy one obtains the Ginzburg-Landau equations from which one can determine the coherence length ξ describing thermodynamic fluctuations of the superconductive phase and the penetration depth λ of an external magnetic field. In 1957 A. Abrikosov used this theory to describe the quantized tubes of flux characterizing type 2 superconductors [82].

The first widely accepted microscopic theory explaining the phenomenon was published 1957 by J. Bardeen, L. Cooper and J. Schrieffer as a macroscopic quantum

mechanical effect and is known as 'BCS-Theory' [83] today. This theory worked for transition temperatures near 0 K and simple alloys, but is not able to fully explain how superconductivity occurs. An electron moving in the lattice of a conductor will cause a slight disturbance of the lattice around it which can attract an opposite spin electron, binding to it with a certain energy and forming a Cooper pair (their binding length is in the range of 200 Å) and forming an energy gap for single particle exitation (instead of no gap in normal metals). If the binding energy is higher than the energy that oscillating atoms of the conductor lattice provide, the Cooper pair stays in the bound state and hence experiences no resistance. A theoretical advancement was the 'Josephson effect' [84] describing the tunnelling phenomenon between two superconductors.

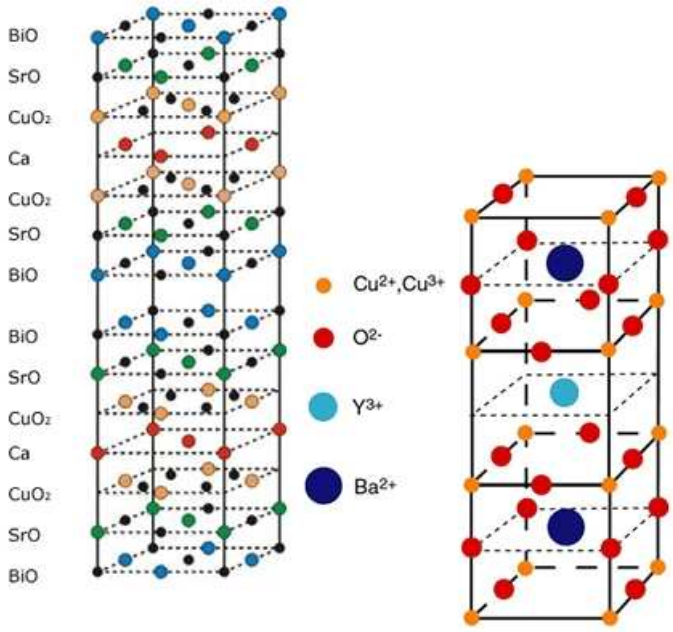

Figure 11: *Crystal structure of high-temperature superconductors BSCCO (left) and YBCO (right). Picture from the world wide web.*

In 1980 K. Bechgaard [85] from the University of Copenhagen synthesized the first organic superconductor, theoretically suggested in 1964 by B. Little [86] from the Stanford University. In 1986 a breakthrough in the field of superconducting materials occurred when A. Müller and G. Bednorz [87] from IBM Rüschlikon observed superconductivity in a ceramic compound made out of lanthanum, barium, copper and oxygen, so called cuprates, having a transition temperature of 30 K.

Following this work many other researchers started to create other ceramics, reaching transition temperatures up to 92 K, when in January 1987 a team from the University of Alabama-Huntsville exchanged the lanthanum against yttrium, to produce the so called YBCO. This was the first time that superconductivity was observed above liquid nitrogen temperature. Using other exotic and even toxic elements,

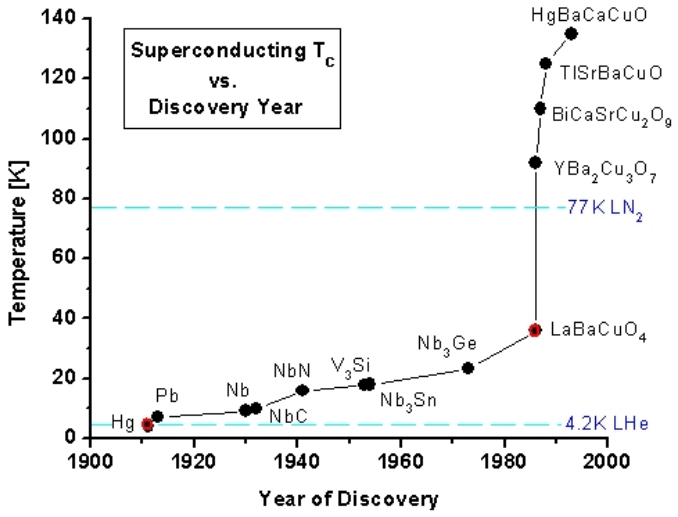

Figure 12: *Discovery of materials with successively higher T_C over the last century. (Points circled in red gave a Nobel Prize for their discoverers). Picture from the world wide web.*

further discoveries were made in the field of perovskite ceramics, these are ceramic oxide materials with a similar crystal structures like $CaTiO_3$, called perovskit. The highest transition temperatures are reached with mercury-cuprates, first synthesized by U. Onbasli in Colorado and A. Schilling, M. Cantoni, J.D. Guo and H.R. Ott [88] in Zürich in 1993. The record today for the transition temperature at normal pressure is 138 K achieved with a thallium doped mercury cuprate in 1994 [89].

Although no significant improvement in the transition temperature occurred since 1994, other discoveries were made, e.g. the existence of superconductive (organic) fullerene (1991) or an alloy of gold and indium that was both superconductive and a natural magnet (1997) or high temperature superconductors that do not contain copper (2000) or the first all-metal perovskite superconductor (2001).

1.3.2 Type 1 superconductors

The so called type 1 superconductors mainly includes metals and metalloids showing normal conductivity at room temperature. They have to be cooled down to a few Kelvin so that atomic vibrations of the lattice are damped enough to provide superconductivity. This is well described with the BCS-theory, which suggests that electrons couple to 'Cooper Pairs', the so called phonon-mediated coupling. This kind of superconductors were discovered first and have a sharp transition to a superconductive state and they are perfect diamagnets, i.e. an external magnetic field is expelled till it reaches the critical value B_C where superconductivity brakes down (see Figure 13).

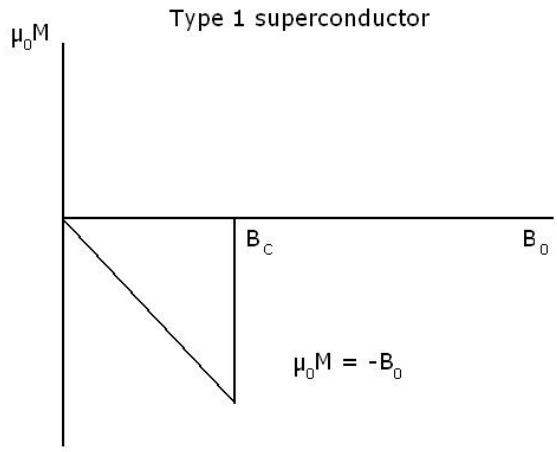

Figure 13: *Influence of an external magnetic field to a type 1 superconductor. The internal magnetization $\mu_0 M$ compensates, and thus, expels the external B-field until the critical field B_C is reached and superconductivity breaks down. Picture from the world wide web.*

1.3.3 Type 2 superconductors

The type 2 superconductors mainly consist of metallic compounds and alloys, except for the elements vanadium, technetium and niobium.

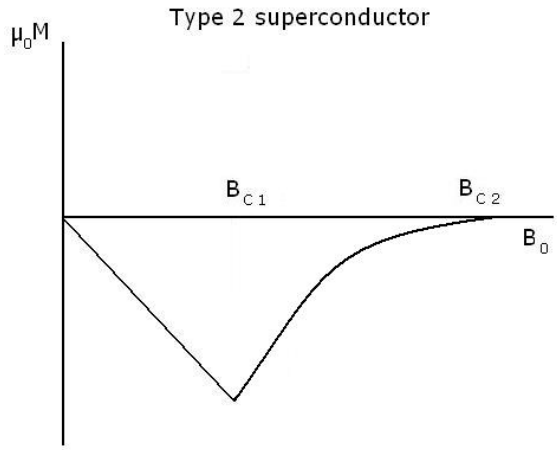

Figure 14: *Influence of an external magnetic field to a type 2 superconductor. The internal magnetization $\mu_0 M$ compensates, and thus, expels the external B-field until the critical field B_{C1} is reached, when quantized fluxes of the external field enter the superconductor material. At a B-field of B_{C2} superconductivity breaks down. Picture from the world wide web.*

The today technically most interesting superconductors like YBCO and BSSCO

are type 2 superconductors. Contrary to the type 1 superconductors they have higher transition temperatures by a mechanism that can not be sufficiently described by any theory yet. The BCS theory, working fine for type 1 superconductors proposes a breakdown of superconductivity for T higher than 40 K due to the too strong lattice oscillations, however temperatures of 135 K are reached. The transition of a type 2 superconductor from normal to a superconductive state is gradual across a region of "mixed state" behavior (see Figure 14). While B_{C1} is mostly small, the difference between B_{C1} and B_{C2} can be big. This is due to the fact that a type 2 superconductor allows quantized fluxes of an external magnetic field to enter into its surface. These fluxes can be pinned via crystal structures, increasing the maximal magnetic field that can be applied. Some theories say the type 2 superconductivity is related to the planar layering of the crystal structure, others suggest that the holes of hypo-charged oxygen are responsible for the superconductive state. Another open question is whether an upper limit for the transition temperature exists or not [90].

1.3.4 Applications

There are many applications for superconductors in industry and science. The most important usage today are electromagnets, especially in the medicine for MRI machines or in particle accelerators, where they are also used for acceleration cavities.

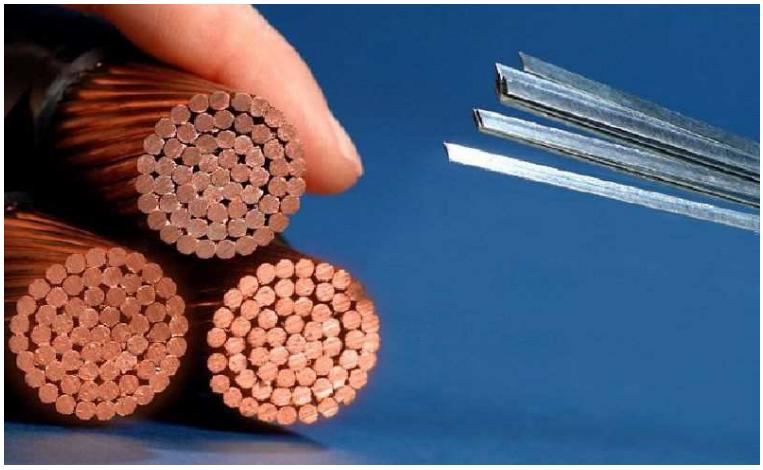

Figure 15: *Comparison of the cross section of a normal conducting wire and a HTS wire carrying the same current (low temperature, no external field). Picture from AMSC.*

Other applications are in the field of high-performance transformers, power storage devices and regulators (i.e. superconductive flywheel systems), electric power transmission, electric motors (e.g. for ship propulsion developed by American Su-

perconductor[2] (AMSC) [91]), magnetic levitation devices [92]. Another possibility is the usage of HTS material as so called SQUIDs (superconductive quantum interference devices), which are very sensitive magneto-meters.

1.3.5 High temperature superconductor (HTS) wires

The breakthrough of high temperature superconductors in industrial processes is closely related to the mass fabrication of HTS wires. Several firms in the USA, Japan and China manufacture HTS wires based on BSCCO 2223, a commonly used name to represent the HTS material $Bi_{(2-x)}Pb_xSr_2Ca_2Cu_3O_{10}$, which are called first generation wires.

Figure 16: *View of the production hall (upper left and right) and the HTS wire at different steps of the manufacturing process (lower left) and the finished HTS wire. Picture from AMSC.*

Generally one can say that first generation wires are produced by milling an alloy pipe of about 6 cm thickness to 4mm wide and 0.2mm high cables. The alloy matrix contains strings of BSCCO powder embedded in a silver tube (see Figure 16). Afterwards the wire is sintered and tempered so that the string of the BSCCO powder forms uniform crystals, which are the superconductive filaments shown at the lower left picture of Figure 17, more details of the production process like the used pressure and temperature are corporate secret. The critical current of the HTS BSCCO wire is strongly dependent on the applied magnetic field and the temperature, it will be discussed for liquid nitrogen (77 K) and liquid argon (87 K) temperature later in this thesis.

[2]HTS Wire Manufacturing Facility, Jackson Technology Park, 64 Jackson Road Devens, MA 01434-4020

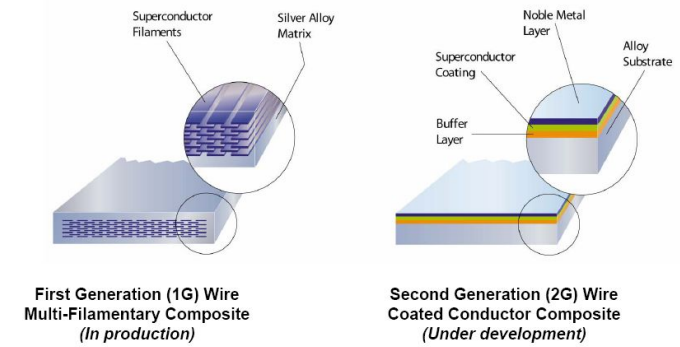

Figure 17: *Comparison of the cross section between a multi-filamentary first and a coated second generation HTS wire. Picture from AMSC.*

HTS wires based on YBCO 123 (or YBaCuO, a ceramic material $YBa_2Cu_3O_{7-x}$, x smaller than 0.5) show a better performance in a magnetic field, as shown in Figure 18.

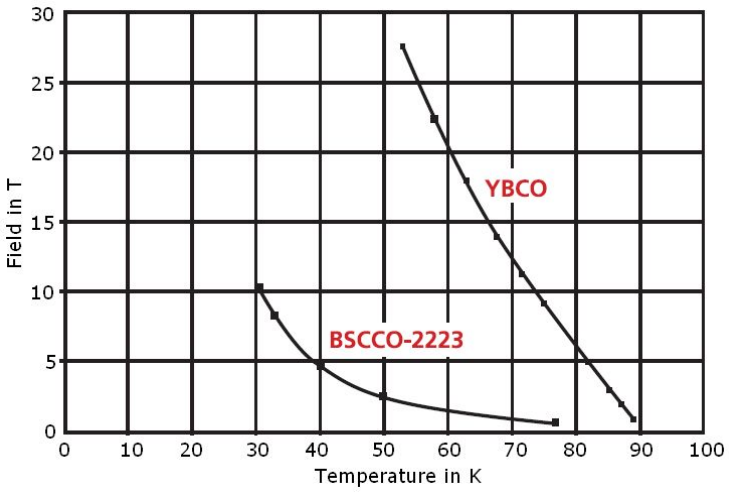

Figure 18: *Plot of maximal applicable magnetic fields for BSCCO 2223 and YBCO, for magnetic field orientation perpendicular to the superconductive CuO planes. Picture from AMSC.*

Figure 19 shows the schematic production process. The production is more difficult, several tempering and surface treatments are needed to produce the wire, the increasing costs are handled by improving the output capacity when producing not only 0.4 cm wide tapes like done for the first generation but 4 cm wide tapes which can be cut into smaller tapes of only 0.4 cm width. Therefore, the production quantity increases by a factor 10, which also reduces the production cost per meter and makes this wires cheaper to trade.

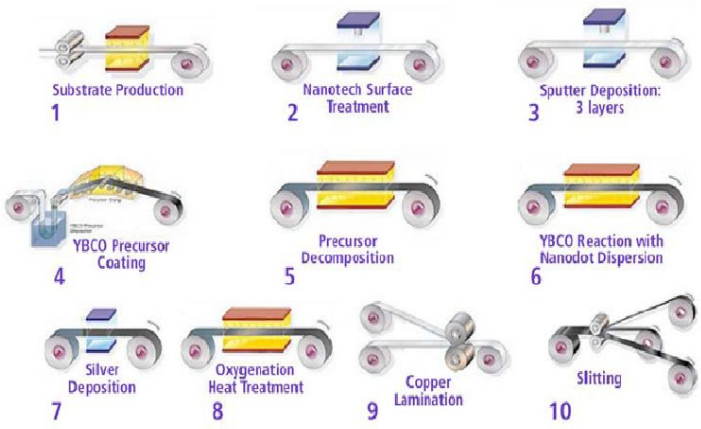

Figure 19: *Schematic view of the production process for the second generation HTS YBCO wire. Picture from AMSC.*

The HTS wire cross section for the second wire generation is shown in Figure 20. On a metal-alloy substrate different layers are coated to allow an easy growth of the superconductive YBCO layer sealed with a silver layer of the same thickness (1 μm). The second wire generation based on the YBCO technology is already in pre–manufacturing state and first wires can be ordered.

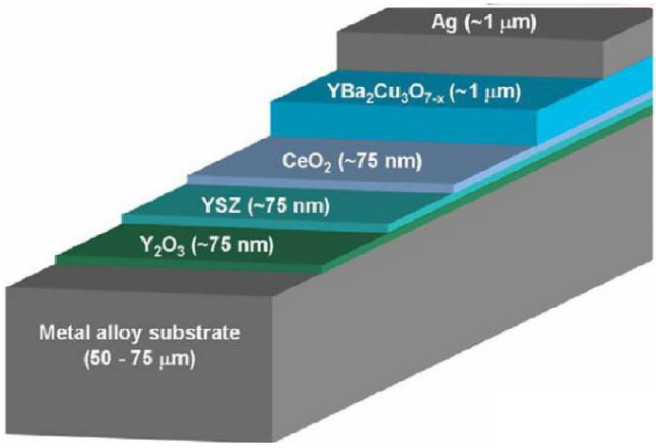

Figure 20: *Cross section view of the second generation HTS YBCO wire. Picture from AMSC.*

First tests showed, that these second generation wires will not only be cheaper, but will also have an outstanding performance, especially in magnetic fields, compared to the first generation wires.

The performance can be improved when so called nanodotted wires are used; these are wires where the magnetic flux is pinned via Yttria (Y_2O_3) nanodots, see Figure 21 for an electron micrograph of the nanodots.

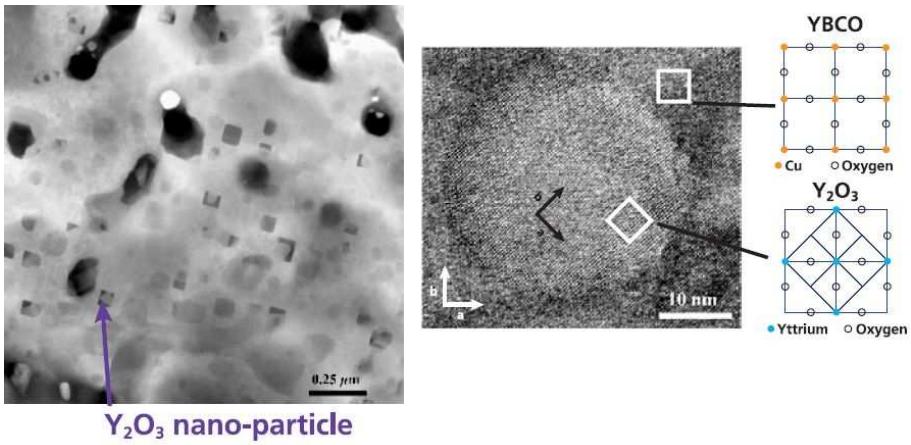

Figure 21: *Electron micrograph pictures of Yttria (Y_2O_3) nanodots in the YBCO matrix. Picture from AMSC.*

Figure 22 shows a comparison of the critical current of second generation wires with and without nanodots when applied to a parallel magnetic field.

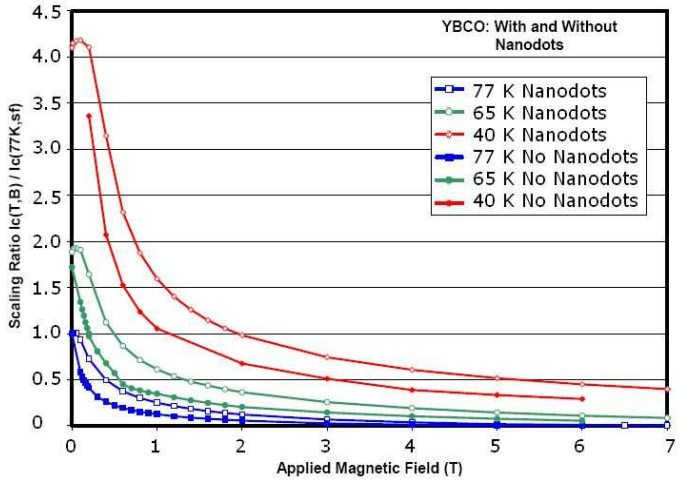

Figure 22: *Comparison of the critical current of second generation wires with and without nanodots when applied to a parallel magnetic field, Picture from AMSC.*

Being in contact with American Superconductor (AMSC) we received a BSSCO 2223 based HTS wire sample of 10 m length for testing. Since the usage of pressurized liquid argon was intended, a hermetic HTS wire was used, i.e. the HTS

wire was hermetically sealed to avoid ballooning effects in the layer of the BSSCO crystals during the rewarming: due to the sintering and tempering process many voids exist in the layer giving room for the liquid gases to penetrate the wire, and during the warming up, the expanding gas destroys the layers (see Figure 23) [93].

Figure 23: *Comparison of the cross section of a normal HTS wire (right) and a HTS wire damaged via ballooning (left). Picture from Sumitomo Electric Industries, Ltd. (SEI).*

2 Magnetic Field Calculations

2.1 Estimating the critical current at LAr temperature

For the BSSCO 2223 HTS wires manufactured by AMSC, the data sheet contains the critical current I_C as a function of the temperature up to the liquid nitrogen (LN_2) temperature of 77 K (at 1 at); since the critical current is very sensitive to the magnetic field at the wire, it is plotted for different perpendicular and parallel field components [94]. The wire is more a ribbon with a rectangular cross section, parallel applied fields therefore mean parallel to the longer side of the rectangular (i.e. the width of the wire), while perpendicular means parallel to the height. The critical current is defined as the current value for which the resistance of the wire reaches 1 μV/cm. No data were available from the manufacture for temperatures above 77 K. Since we are interested in the behaviour of the HTS wire at the LAr temperature of 87.5 K (at 1 at), the curves from the data sheet were extrapolated to higher temperatures, fitting the data points from the data sheet with a logarithmical fit (or for one case a polynomial fit of order 2); for B= 0 T the point with I_C= 0 A at the (critical) temperature T=110 K was added for the fit [97]. Figures 24 and 25 show the results of the fits for perpendicular and parallel (external) magnetic fields. Figures 26 and 27 show an expanded view around the boiling temperature of argon of 87.5 K (at 1 at).

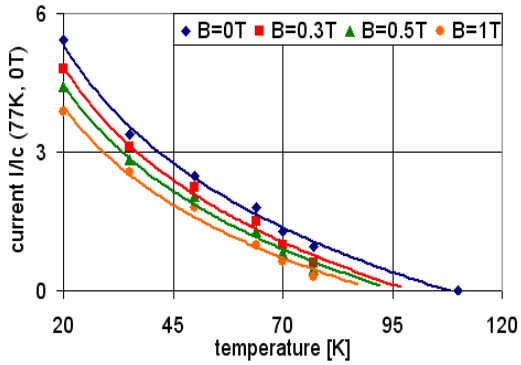

Figure 24: *Critical current (relative to I_C at 77 K) for different values of a parallel magnetic field as a function of the temperature. The curves are fits to the data points read from the data sheet.*

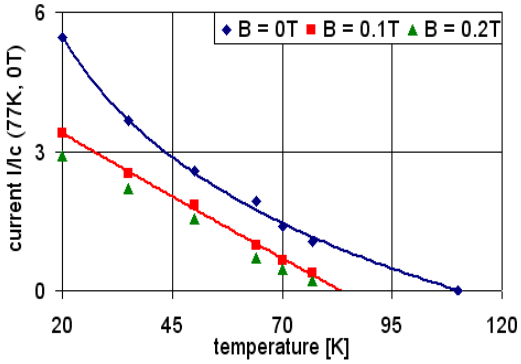

Figure 25: *Critical current (relative to I_C at 77 K) for different values of a perpendicular magnetic field as a function of the temperature. The curves are fits to the data points read from the data sheet.*

For no external magnetic field the critical current at LAr temperature is about 65% (i.e. 97 A) of its 77 K value of 149 A. For a parallel magnetic field the critical current as a function of the temperature can be approximated by an logarithmic function. Assuming a parallel field of 0.25 T, the critical current is about 45 A, i.e

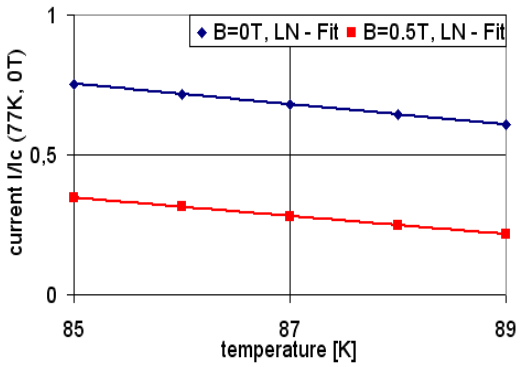

Figure 26: *Expanded view of Figure 24 around the liquid argon temperature.*

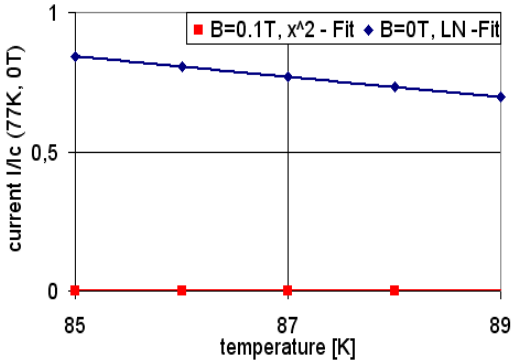

Figure 27: *Expanded view of Figure 25 around the liquid argon temperature.*

50% of the value without field. For a field of 0.5 T the critical current is only 22 A, i.e. 20% of its value without external field.

An external perpendicular field through the HTS-wire strongly reduces the critical current, even for a 'small' field of only 0.1 T no superconductivity occurs, i.e. the critical current I_C is zero. Therefore, to achieve a magnetic field as high as possible with a HTS solenoid, the design has to be optimized. Higher currents increase the B-field on the one hand, but on the other hand they reduce the critical current I_C of the HTS wire. A yoke should be used to reduce the influence of a perpendicular magnetic field to the HTS wire.

2.2 Estimating the magnetic field on the solenoid symmetry axis

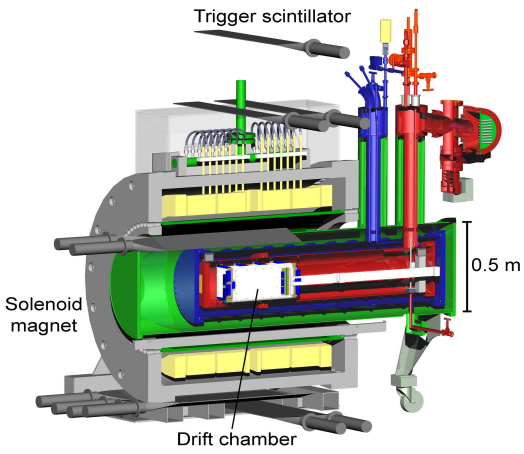

Figure 28: *CAD draft of the LAr TPC setup with the SINDRUM-I magnet. Picture from [6].*

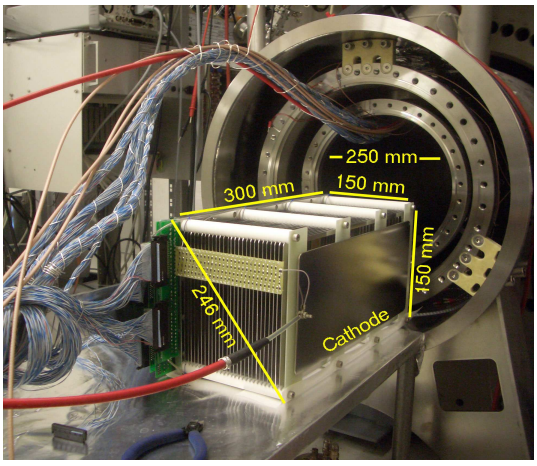

Figure 29: *Picture of the open dewar and the LAr TPC (cuboid in the front). Picture from [6].*

2.2.1 The solenoid geometry

The motivation for this diploma thesis is to use a HTS solenoid with a small LAr TPC. A full description of the TPC setup is given in [6] and a draft is shown in Figure 28. The LAr TPC is situated in a dewar with a cylindrical shape and a radius of 12.5 cm. The TPC is a cuboid shape with a length of 30 cm and a quadratic front of 15 cm side length (see Figure 29). HTS wires are very sensitive to bending too, therefore the optimal solenoid structure is cylindrical, i.e. the maximum radius is 12.5 cm. The minimum radius was given by the minimal bending radius of the HTS wire of 5 cm (by the manufacturer) and the fact that the existing chamber can only be scaled down slightly, leading to a minimum radius of about 10 cm. Given a radius of 10 cm to 12.5 cm less than 80 cm of wire is needed for each turn of the coil. For practical reasons (cost of the HTS wire, delivery times of the HTS wire manufacturer) the wire length should be kept below 1 km.

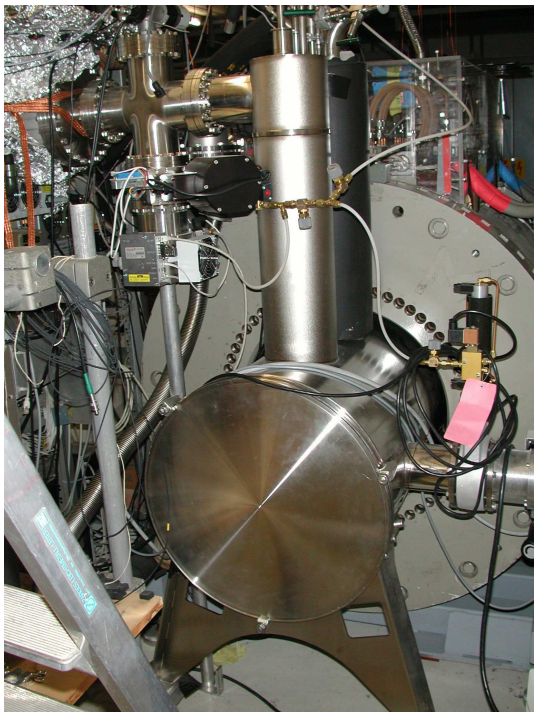

Figure 30: *Picture of the LAr cryostat from the front. The pipes containing the read-out cables and HV-supply can be seen. On the left a part of the data acquisition system is shown.*

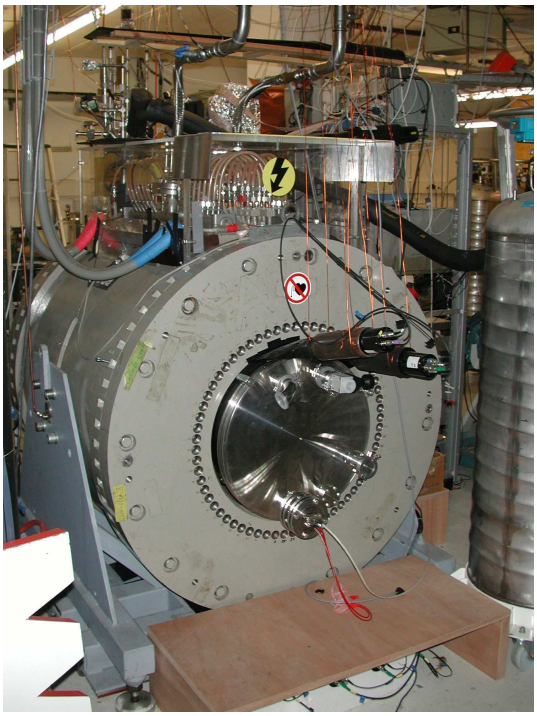

Figure 31: *Picture of the LAr cryostat from the back. The grey ring is the recycled SINDRUM-I magnet with the cooling water supply on top. The trigger scintillators for cosmic rays can be seen too.*

For first calculations a coil with a fixed number of 1000 turns was assumed, so that the total wire length was less than 800 m. The HTS-wire has an average thickness of 0.39 mm and an average width of 4.39 mm, thus, first calculations were made for a cross section of 0.4 mm x 5 mm per wire. For a fixed number of 1000 turns, the

total cross section of the solenoid was 20 cm^2 (2 mm$^2\times$ 1000 turns). Depending on the radial thickness of the wire winding one could vary the length of the solenoid (e. g. a thickness of 0.5 cm leads to a length of 40 cm for the solenoid with 1000 turns). To get a first impression of the field strength that could be achieved with a wire length of $\lesssim$ 1 km a circular winding with an inner radius of 10.5 cm and an outer radius of 12.5 cm was assumed, i.e. the HTS-wire is wound to a cross section with a length of 10 cm and a radial thickness of 2 cm.

2.2.2 Calculating the field

Three different formulae [95] were used to calculate the magnetic field on the axis. The current in all 3 cases is I=45 A per turn (critical current chosen from the estimation of chapter 2.1 for B=0.25 T), i.e. for the N=1000 turns the total current is IN=45'000 A, while μ_0 is the permeability of the vacuum.

1. Solenoid consisting of 1000 loops with negligible extensions:

$$B(x) = \frac{\mu_0 I N r^2}{2(r^2+x^2)^{\frac{3}{2}}} \tag{3}$$

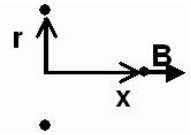

Figure 32: *Loop of a radius r, x is the ordinate on the axis.*

2. Thin solenoid of radius r and length l:
   $x_1 = x - \frac{l}{2}$ and $x_2 = x + \frac{l}{2}$, where the origin of x is in the center of the solenoid.

$$B(x_1, x_2) = \frac{\mu_0 I N}{2l}\left(\frac{x_2}{\sqrt{x_2^2+r^2}} - \frac{x_1}{\sqrt{x_1^2+r^2}}\right) \tag{4}$$

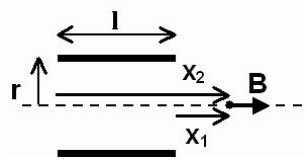

Figure 33: *Geometry and parameters of a thin shell solenoid.*

3. Solenoid with a radial thickness d and a length l:
   x_1, x_2 (see 2.), r_1 - inner radius and r_2 - outer radius

$$B(x_1, x_2) = \frac{\mu_0 IN}{2l(r_2 - r_1)} \left(x_2 \ln \left(\frac{\sqrt{x_2^2 + r_2^2} + r_2}{\sqrt{x_2^2 + r_1^2} + r_1} \right) - x_1 \ln \left(\frac{\sqrt{x_1^2 + r_2^2} + r_2}{\sqrt{x_1^2 + r_1^2} + r_1} \right) \right) \tag{5}$$

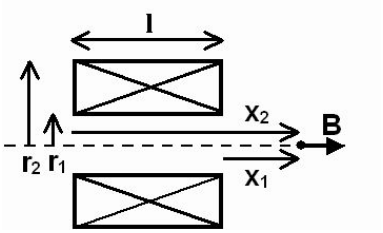

Figure 34: *Geometry and parameters of a thick shell solenoid.*

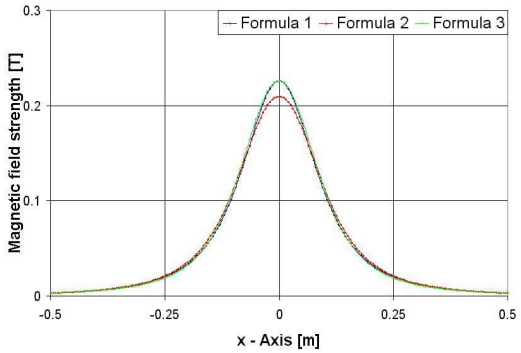

Figure 35: *Calculated magnetic field on the solenoid axis for 1000 turns and I=45 A per turn. Length of the coil l=10 cm and the radius r=10.5-12.5 cm, see text for more details.*

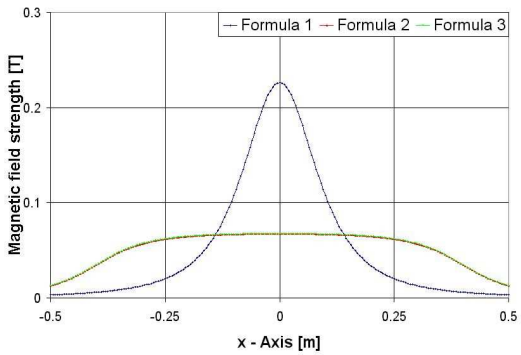

Figure 36: *Calculated magnetic field on the solenoid axis for 1000 turns and I=45 A per turn. Length of the coil l=80 cm and the radius r=12.25-12.5 cm, see text for more details.*

Figure 35 shows the magnetic field on the x-axis for the following parameters: Total current IN=45'000 A, length (formula 4 and 5): l=10 cm, radius (formula 3 and 4): r=12.5 cm and radii (formula 5): r_1=10.5 cm, r_2=12.5 cm
For the short solenoid with a length of l=10 cm length all calculations gave similar results: with a solenoid made out of 1000 turns one could expect to generate a field up to 0.2T with a current of 45 A per turn. From chapter 2.1 the current of 45 A is the critical current for a magnetic field of 0.25 T, but changing the current changes the magnetic field. Higher currents produce a higher magnetic field reducing the critical current below the value of 45 A. They are therefore not applicable, so I_C=45 A is the best choice.

Figure 36 shows the magnetic field on the x-axis for a longer and thinner solenoid with the following parameters:
Total current IN=45'000 A, length (formula 4 and 5): l=80 cm, radius (formula 3 and 4): r=12.5 cm and radii (formula 5): r_1=12.25 cm, r_2=12.5 cm
The length of the solenoid begins to have an effect on the calculation, it is clearly visible that formula 3 gives a high peak-like field over a distance much shorter than the solenoid length and is therefore not a good approximation -as expected- to calculate the field for extended solenoids while the other two formulae 4 and 5 give the same results. An extended solenoid without yoke has a magnetic field of 0.07 T (I=45 A per turn, 1000 turns).

2.3 2D Simulation of the magnetic field

For the now known current and the constraints for the solenoid cross section the first design ideas for the solenoid were made. The previous formulae gave only information about the on axis field of a coil. For the TPC the whole volume has to have a high magnetic field. Thus, two dimensional calculations had to be made (although the volume is three dimensional, the cylindrical shape allows a two dimensional view due to the rotation symmetry).

2.3.1 The software program Elefant2d

Assuming cylindrical symmetry of the solenoid a two dimensional simulation of several layouts for the solenoid with the software 'elefant2d' was made. This software was developed by Istvan Bardi, Oszkar Biro and Kurt Preis from the Institute for Fundamentals and Theory in Electrical Engineering, TU Graz (Austria)[96]. For this program the homogeneous total current through the cross section of the coil (length × radial thickness) has to be given. The assumed wire length was again 800 m. Again the outer radius was restricted to 12.5 cm, so that a coil with a cross section of 10 cm × 2 cm had an inner radius of 10.5 cm. The longer the magnet, the smaller is the calculated maximal field strength in the center for a fixed number of 1000 turns; a thick short magnet has the advantage of a high central field, while the thin, extended magnet offers a longer homogenous field distribution. Another possibility to achieve homogeneous fields is the use of a Helmholtz coil design, thus several Helmholtz like geometries were simulated, having altogether 1000 turns, i.e., each single coil was made of 500 turns. The results of the simulations are presented in figures indicating the position of the coils and the field lines and giving the field strength with a color code. The left edge of the pictures represents the cylindrical symmetry axis, called x-axis, while the bottom edge of the pictures is the parallel r-axis.

2.3.2 Helmholtz coil without yoke

For the first simulation a Helmholtz coil design with a radius of 10.5 cm and a gap of 2.5 cm between the coils was used, assuming each single coil having a cross section of 5 cm x 2 cm, i.e. 500 turns and applying a current of 45 A, giving a total current of 22'500 A for each coil (i.e. 45'000 A altogether). Figure 37 shows that the calculated field is not very homogenous in the outer regions but achieves a field strength up to 0.2 T on the symmetry axis. To gain more information about the field, radial, axial and absolute field strength along several paths through the solenoid were plotted. The most interesting information comes from the path along the inner surface of the solenoid, since there are the highest fields to which the HTS wire is exposed. Figure 37 shows the resulting field with indicated field lines and the color coded field strength. The simulation showed that the highest perpendicular field strengths occur on the inner coil surface, decreasing the estimated critical current to zero.

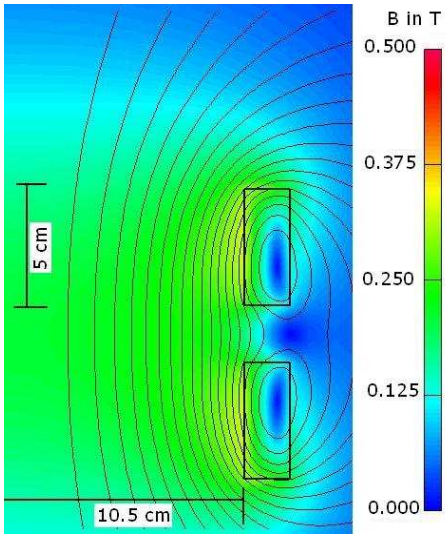

Figure 37: *2D field calculation for a Helmholtz coil design. Each coil has 500 turns and I=45 A per turn.*

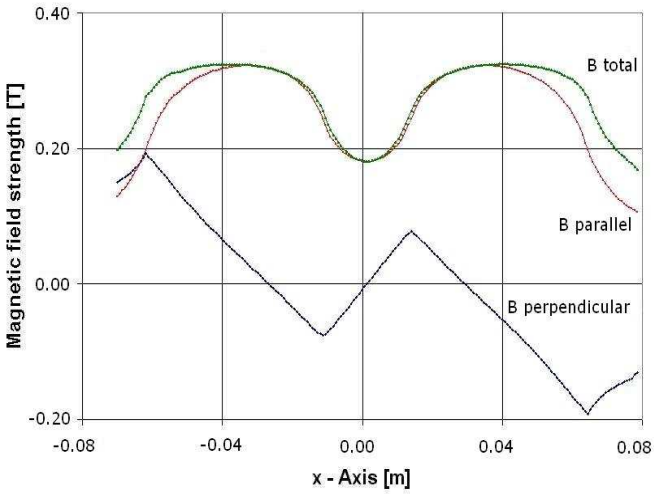

Figure 38: *Helmholtz coil design, magnetic field component $B_{parallel}, B_{perpendicular}$ and total field strength $|B_{total}|$ along the inner surface of the coils (500 turns, I=45 A per turn).*

Another disadvantage was that the test chamber has a length of 36 cm, making a coil of this structure too small to be of use when designing our magnet. Changing the gap to 5 cm, the field decreases to less than 0.2 T in the center of the magnet and with a gap of 10 cm an even longer homogenous field was calculated but it had a lower field strength in the center of the magnet. Unfortunately, the perpendicular fields on the solenoid surfaced were not decreasing a lot, so that the critical current would still be reduced to zero. Therefore, a current of less than 45 A had to be applied. Changing the geometry of the single coils, the field on axis was even smaller than in the geometries before, therefore, no further investigations for the Helmholtz coil design were pursued.

2.3.3 Single solenoid without yoke

A cylindrical solenoid with an inner radius of 8.5 cm and a coil cross section of 5 cm (length) × 4 cm (thickness) was used for the first simulation, so that the total cross section was 20 cm^2 for 1000 turns of the wire, i.e. the total current was still 45'000 A. Figure 39 shows that the calculated field was not very homogenous over a long distance but a field strength up to 0.4 T was achieved near the solenoid surface. Again the field strength along several paths through the solenoid was plotted and the most interesting information came from the path along the inner surface of the solenoid. This solenoid design had a magnetic field on the x-axis up to 0.5 T, but the radial thickness would decrease the size of the chamber too much, so another design had to be selected. Another disadvantage can be seen from Figure 40: high perpendicular fields at the inner coil surface decrease the critical current to zero.

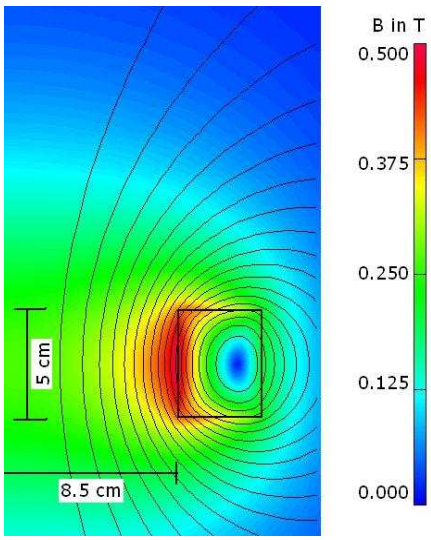

Figure 39: *2D field calculation for a single solenoid design. The coil has 1000 turns and I=45 A per turn.*

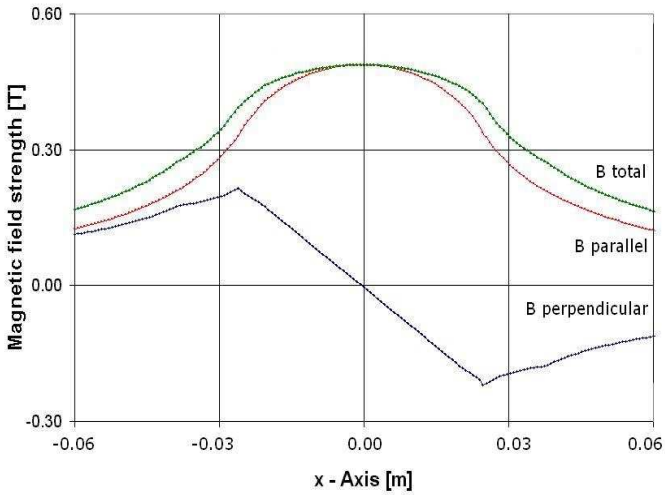

Figure 40: *Single solenoid design, magnetic field component $B_{parallel}, B_{perpendicular}$ and total field strength $|B_{total}|$ along the inner surface of the coil (1000 turns, I=45 A per turn).*

Simulation of other cross sections like 10 cm × 2 cm showed that the homogeneous field area could be increased with a field strength of 0.25 T, but still high perpendicular fields through the surface of the coil existed, decreasing the critical current to zero like before. Other cross sections like 20 cm × 1 cm had a homogeneous field over a longer distance, but now only a field strength of 0.18 T was achieved and again the high perpendicular field through the surface of the coil decreased the critical current to zero. All simulations showed that too high perpendicular fields occurred to apply a current of 45 A. Therefore, a yoke was added to find a solution for this problem.

2.3.4 Adding a yoke

Adding an iron yoke to the 10 cm × 2 cm coil, the first simulation showed that even extended coil geometries like 20 cm x 1 cm provided a field that was high enough for our purposes. The TPC has an outer length of 36 cm, leading to an overall length for the solenoid of 40 cm with a cross section of 40 cm × 0.5 cm for the coil. For the first simulations an outer yoke with an average thickness of 1 cm was assumed, i.e., the inner radius of the solenoid was 10.9 cm, leaving a distance of 0.1 cm between coil and the yoke. Figure 41 shows that a simple yoke already provides a very homogenous field with a field strength of about 0.14 T for a total current of 45'000 A. Thanks to the yoke no high perpendicular field occurred on the surface of the coil, the perpendicular magnetic field strength was less than 0.004 T, i.e. the critical current will be limited by the parallel component of the field in this configuration. Further simulations were made changing the cross section of the coil to achieve higher fields in the center of the solenoid. This simulations, shown in Figure 42 shows e.g. the results with a trapezoidal coil cross section (I=45 A) resulting in a magnetic field of 0.25 T in the cental region.

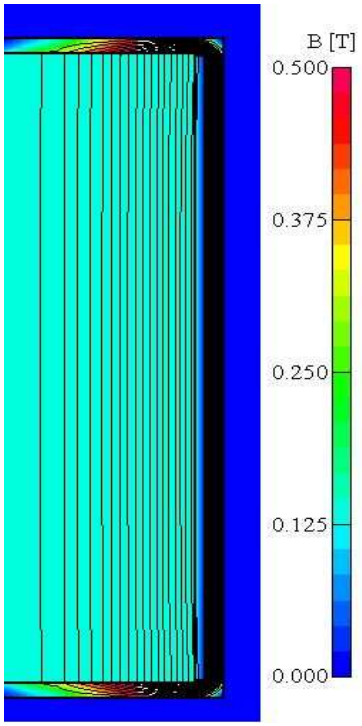

Figure 41: *2D magnetic field simulation of a solenoid with an added yoke, having a cubic cross section of 40cm length and 0.5cm radial thickness for 1000 turns and I=45 A per turn.*

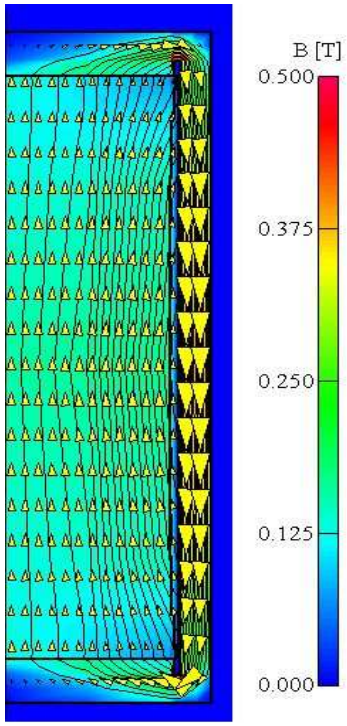

Figure 42: *2D magnetic field simulation of a solenoid with an added yoke, having a trapezoidal cross section of 0.5cm radial thickness, an inner length of 20cm and an outer length of 40cm for 1000 turns and I=45 A per turn.*

Note that the values for the critical current are the result from the extrapolation of the data sheet and have to be determined in experiments since no simulations could show the realistic behavior of the HTS wire at the temperature of liquid argon. Modulating the mirror plate for a trapezoidal cross section did not show a big effect on the field strength. The simulations also showed that the magnetic field strength inside the yoke material was about 0.4 T to 0.45 T , this was far away from the saturation field strength of the yoke material (about 1.8 T for annealed steel). Therefore, the outer yoke can be thinner than simulated, i.e. the TPC had to be less scaled down. An optimized solution can be searched later, when the critical current is better known.

The simulations showed that a solenoid with a cross section of 40 cm $\times$ 0.5 cm consisting of 1000 loops produces a magnetic field of 0.2 T when equipped with a yoke and supplied with a current of 45 A. A solenoid with these properties would require 800 m of HTS wire. Due to the assumed dimensions, the solenoid would fit in the existing LAr TPC setup and could contain the existing TPC (which has to be modified slightly). Higher currents (with the corresponding higher fields) would decrease the critical current I_C and are therefore not applicable in this configuration. Since the dependence of the critical current on the magnetic field is just estimated from extrapolations of the data sheet (see chapter 2.1), measurements investigating this dependence have to be made.

3 Measurements with a short HTS wire

The first problem to be solved was the connection between the HTS wire and the power supply. From the estimation of chapter 2.1 the expected critical current I_C was 100 A at LAr temperature (B=0 T, 1 at). To supply the HTS wire with such a current, it had to be connected with a power supply by a normal conducting cable, since the HTS wire was not capable to transport a current of 100 A at room temperature. Only when being a superconductor the HTS wire can carry higher currents than normal copper wires, since in the superconductive state it has a current density that is much higher than for normal copper wires. The connection between normal and HTS wire has to have a low resistivity to avoid heating up at high currents, since that could affect the superconductive properties of the HTS wire.

3.1 Connecting the HTS wire to the power supply

To obtain a good connection between the HTS wire and the (normal conducting) cable from the power supply, the contact should be over a large area of 1 cm^2 [98]. To carry a current of 100 A to the HTS wire a copper cable with a cross section of 25 mm^2 was used. The HTS wire was spliced to a copper block shown in Figure 43, and the copper cable was was screwed (M6) with a lug on the block.

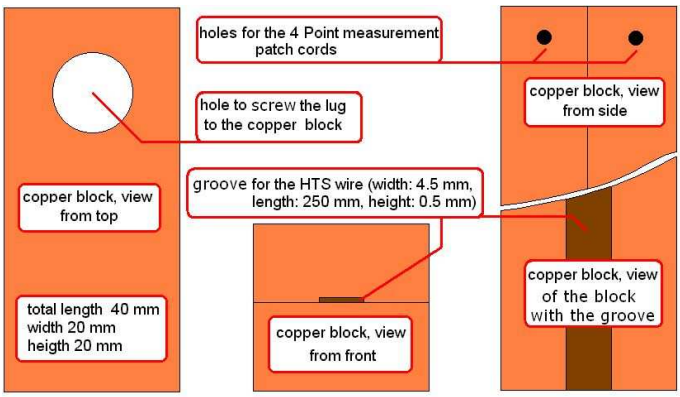

Figure 43: *Draft of the copper block connection between the HTS wire and the normal conducting wire.*

The block consists of two halves, with a 25 mm long groove for the HTS wire in one halve (see Figures 43 and 44. It is important to use low temperature solder in order not to damage the solder sealing of the HTS wire (PbSn, melting point 187° C). With a damaged seal LAr could penetrate into the voids of the superconductor leading to the ballooning effect described in section 1.3.5 when the HTS wire is warmed up, destroying the superconductor. To splice the HTS wire to the copper block an indium solder with a melting point of about 160° C was chosen.

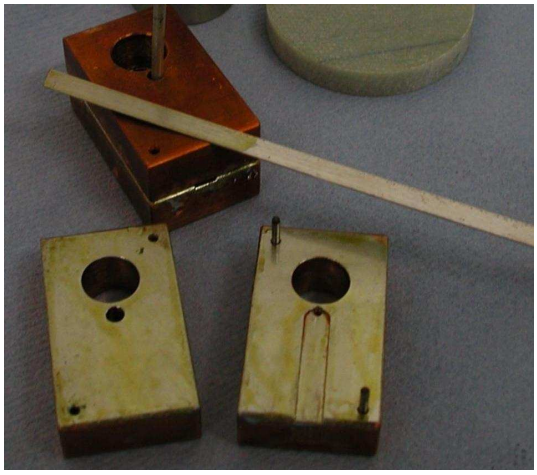

Figure 44: *Two halves of a copper connection showing the groove and the soldered surface.*

A soldering flux based on resin was used to allow a better flow of the indium. Another improvement of the indium flow was achieved by cleaning the copper block in 10% HCl solution and soldering it with a PbSn layer. The soldering was done on a temperature controlled hot plate. For the first measurements to determine the critical current in LAr or LN_2 with and without magnetic field, a 15 cm long wire sample was used and soldered to the two copper block on both ends.

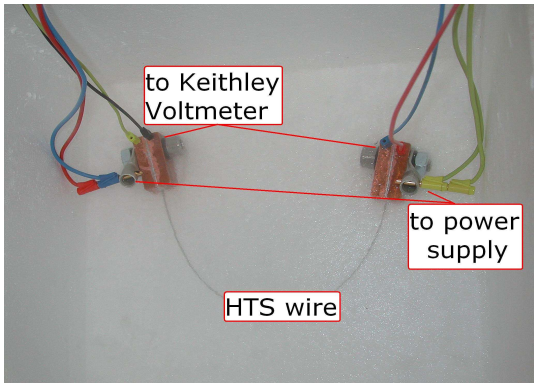

Figure 45: *Experimental setup for the 4-point measurement of the HTS wire resistance in LN_2.*

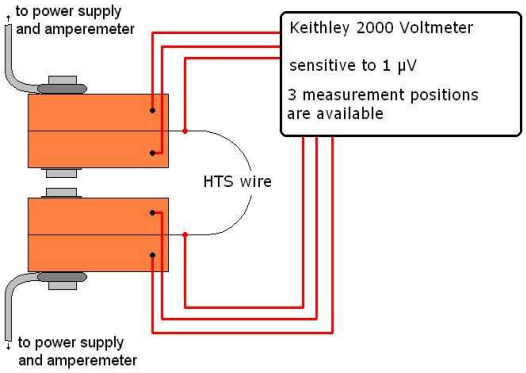

Figure 46: *Schematic view of the 4-point measurement of the HTS wire resistance in LN_2.*

The HTS wire sample and the copper connections were cooled with LN_2 to 77 K when connected to a 8 A power supply to measure the resistance of the connection as shown in Figure 45. For a first test a small power supply with a current of 8 A was connected with some patch cords as test leads. The current was measured with the ampere-meter of the power supply. The voltage drop, either across the HTS wire alone or including the copper connections, was measured with a Keithley

2000 multi-meter (4-point measurement, see Figure 46). To eliminate the effect of thermoelectric potentials, the polarity was switched at the power supply. If a resistance exists in the HTS wire, a voltage can be measured in accordance to Ohm's law ($U = R \times I$). If the HTS wire enters a superconductive state, its resistance becomes zero and no voltage appears. Measuring over the copper blocks allows the determination of the connection resistance. The total resistance through the copper blocks and the HTS wire was about (0.3±0.1) $\mu\Omega$ applying a current of 8 A. To get more information the Mk2 power supply from Oxford Instruments with a maximal current of 70 A was used for the following measurements[3].

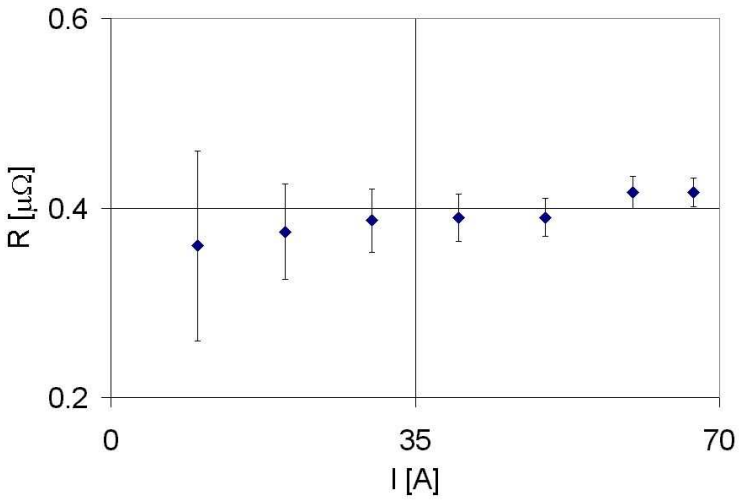

Figure 47: *Measured resistance of the HTS wire with both copper connections at LN_2 temperature for different currents.*

This time the power supply cable had a larger cross section of 25 mm^2, the rest of the setup stayed the same. At room temperature the measured voltage drop over the copper blocks and the HTS wire was 43 mV at a current of 7.5 A, so the resistance was 6 mΩ. Cooling down the probe with LN_2 this resistance became 0.4 $\mu\Omega$ (see Figure 47). Measuring only the resistance of the HTS wire at LN_2 temperature , i.e. without the copper block, no voltage drop was measurable, thus, the voltage drop was below 10^{-6} V, which is the limit of the used Keithley voltmeter. The total voltage provided by the power supply at a current of 50 A was 246 mV, i.e. the complete setup, including the supply cables, had a resistance of 4.92 mΩ when the HTS wire was cooled to a temperature of 77 K.

The measured resistance of the copper blocks and the contact resistance between copper block and HTS wire of 0.4 $\mu\Omega$, creates a heat input of less then 1.4 mW for a current of I=60 A, which is negligible.

[3]We thank K. Mattenberger from the Institute for Solid State Physics of ETH for lending us the power supply.

3.2 Test of the HTS wire in a magnetic field

The critical current I_C of the used HTS wire is not only dependent on the temperature but also strongly affected by a magnetic field. The dependence on the B-field is different for parallel and perpendicular magnetic fields applied to the wire (see HTS wire data sheet [94]). This effect has to be studied in more detail for the HTS wire used for the solenoid, since the solenoid will produce a magnetic field affecting the HTS wire coil.

3.2.1 Test with permanent magnets

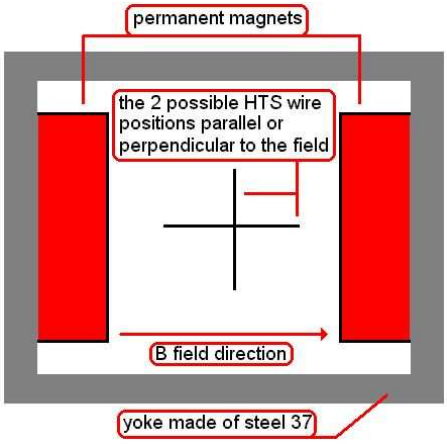

Figure 48: *Schematic view of the yoke setup for small permanent magnets, total length 30 mm, width and height 20 mm, B=0.2 or 0.4 T.*

The first test to get an idea about the influence of an external magnetic field on the critical current of the HTS wire was to put different permanent magnets next to the wire and measure the expected changes in the voltage drop. A small yoke made out of several steel 37 pieces was built so that the applied field had only an influence on the wire over a the length of the permanent magnet. The HTS wire could either be positioned parallel or perpendicular to the magnetic field of the permanent magnets (in Figure 48 the setup is shown). Different pairs of permanent magnets were used, the first pair had a diameter of 1.3 cm and a field strength of 0.34 T at room temperature, increasing to 0.4 T at 77 K. The second pair of magnets had a diameter of 1.8 cm and a field strength of 0.2 T at 77 K and nearly the same value at room temperature. The magnetic field at LN_2 temperature was measured by taking the cooled yoke with the permanent magnets out of the liquid nitrogen dewar on a table at room temperature and then the field was measured with a Hall probe as quickly as possible. This measurement was not very exact, since the yoke starts to warm up on the table, but this warming up was only a few degrees and only this method allowed to measure the field without cooling the Hall probe, which was impossible for the used Gauss-meter due to a probe length of only 5 cm.

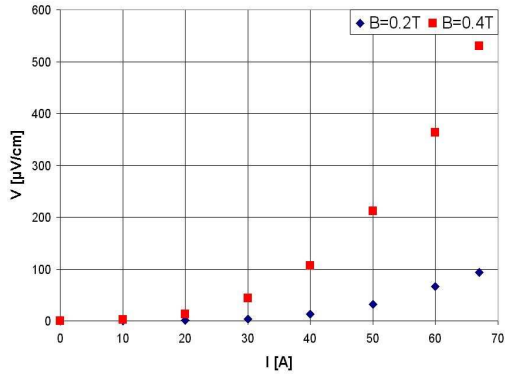

Figure 49: *Measured voltage drop per cm of HTS wire in LN_2 as a function of the current for different perpendicular B-fields (produced by a permanent magnet).*

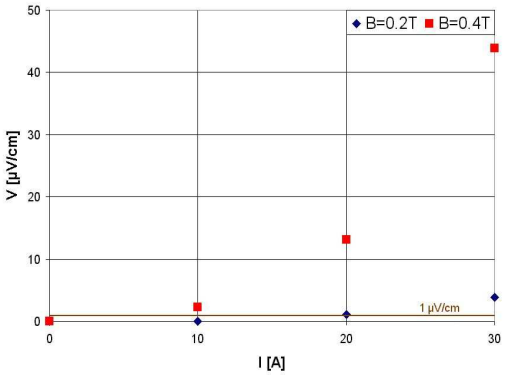

Figure 50: *Expanded view of Figure 49. Measured voltage drop per cm of HTS wire in LN_2 as a function of the current (I=0-30 A) for different perpendicular B-fields.*

As seen in Figure 49, the HTS wire resistance raises nonlinear with the current. The magnetic field applied to the wire over a length of 2 cm caused the superconductivity to break down at this position. A nonlinear resistance-current characteristics is visible. This characteristics is typical for a type 2 superconductor, while a part of the current is still transported via superconductivity, a rising fraction of the current is transported through normal conduction.

The critical current I_C quoted by AMSC produces a voltage drop of 1 μV/cm in the HTS wire (definition of I_C used by AMSC). Therefore, a perpendicular field of 0.2 T has a critical current of 20 A, while for a field of 0.4 T the critical current was less than 10 A (see Figure 50 and [97]). If a higher current than the critical current I_C is flowing through the HTS wire, the increasing resistance causes a heat input; assuming a wire length of l=800 m (see chapter 2.2.1) and a current of 60 A the heating power can be calculated with $P = UI$, where U can be obtained from the measurement shown in Figure 49 with $U[\mu V] = U[\mu V/cm] * l[cm]$. A perpendicular field of 0.4 T causes a heat input of 1.7 kW, a perpendicular field of 0.2 T causes a heating power of 0.3 kW, while a superconductive wire with a resistance of less than 1 μV/cm causes a heat input of less than 4.8 W.

For a parallel magnetic field of 0.2 T no effect to the resistance was visible, the voltage drop over the wire was below 10^{-6} V, and therefore not measurable with the used Keithley voltmeter. For a field of 0.4 T a small effect may have shown up when the current was increased above 60 A, but the measured value of 1 μV is exactly the error limit of the Keithley voltmeter. For the maximal current output of 67 A from the power supply the effect became barely visible, the resistance was 0.1 $\mu\Omega$.

This first test confirmed that perpendicular fields have a bigger effect on the critical current I_C than parallel magnetic fields and should therefore be avoided. Stronger permanent magnets would be needed to investigate the resistance-magnetic

field dependence for parallel magnetic fields. The expected magnetic field strength produced with the solenoid was below 0.3 T (see chapter 2.2), therefore, the influence of a parallel field is negligible in LN_2, but more extensive measurements of the influence of perpendicular magnetic fields below 0.3 T to the resistance were needed.

3.2.2 Tests with a small test coil

Since no tunable magnetic field could be produced with permanent magnets, a small test coil was built. Applying a current from 0 to 8 A a tuneable magnetic field from zero up to 0.14 T was produced (see Figure 52).

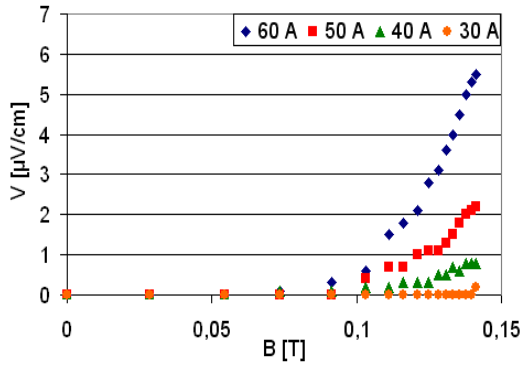

Figure 51: *Measured voltage drop per cm of HTS wire in LN_2 as a function of the perpendicular B-field for different currents.*

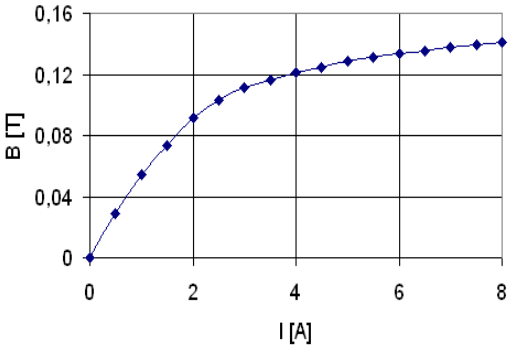

Figure 52: *Magnetic field produced by the small test coil at LN_2 temperature.*

As seen in Figure 51 the superconductivity broke down for perpendicular fields of more than 0.1 T for a current of I=60 A. Smaller currents allowed higher magnetic fields, before the resistance increased. The simulations for the solenoid showed that the produced perpendicular field strength will be less than 0.05 T (see chapter 2.3) for a current of 45 A and using a yoke. Therefore, the effect of perpendicular fields can be neglected in LN_2.

3.2.3 Tests with a big test coil

So far only measurements in LN_2 were discussed. However, the solenoid should be applied to a LAr TPC and therefore the wire will only be cooled to LAr temperature (≈87 K), more than 10 K warmer than the boiling point of LN_2 (≈77 K). Therefore, measurements in both LN_2 and LAr have to be made to compare the influence of magnetic fields (both parallel and perpendicular) at both temperatures. The used coil was a cable roll from the stock (see Figure 53) with a length of 20 cm, which was connected to a small power supply.

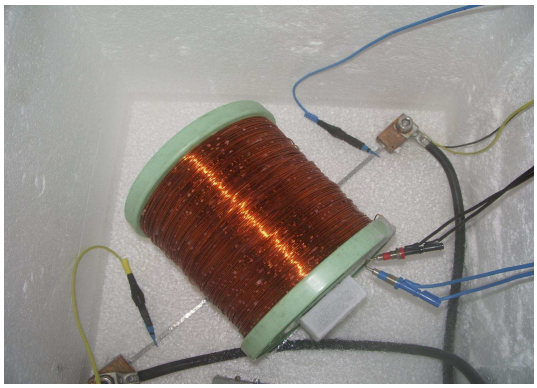

Figure 53: *Experimental setup with the big test coil, see text for details.*

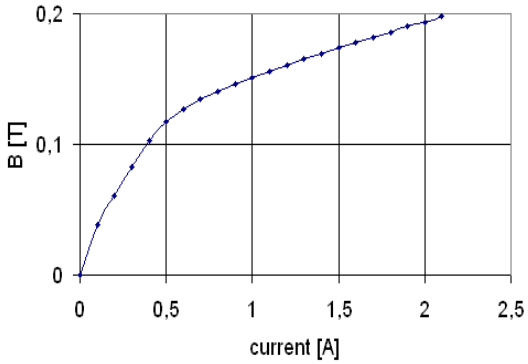

Figure 54: *Magnetic field produced by the big test coil at LN_2 temperature.*

A C-shaped steel 37 yoke was used to have a 5 cm long gap (width 2 cm, gap opening 0.5 cm) between the poles with a homogeneous magnetic field to expose the HTS wire. The gap size was chosen as 5 cm to obtain a more precise measurement of the voltage drop per length than with the former circular gaps having radii between 1 or 2 cm. Due to the yoke the stray fields of the coil were negligible, most of the magnetic flux was absorbed by the yoke. The coil provided a magnetic field tuneable from zero up to 0.2 T (see Figure 54). The HTS wire could be either positioned parallel or perpendicular to the magnetic field.

3.2.4 Measurements in LN_2

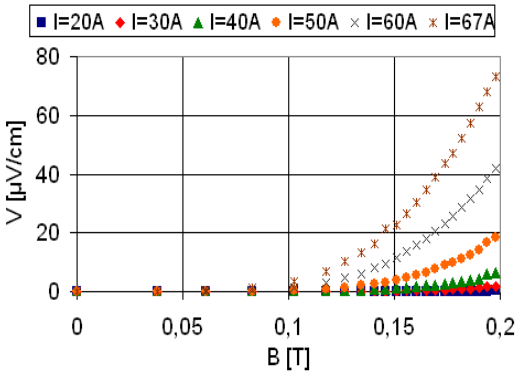

Figure 55: *Measured voltage drop per cm of HTS wire in LN_2 as a function of the perpendicular B-field for different currents.*

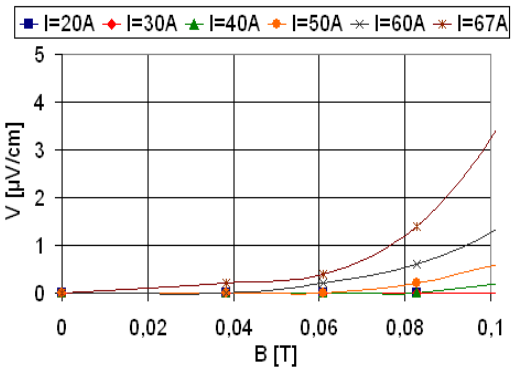

Figure 56: *Expanded view of Figure 55, Measured voltage drop per cm in LN_2 for perpendicular B-fields up to 0.1 T.*

The first measurement with the new coil was made with LN_2. After the break down of the superconductive state, the resistance started to rise linearly while the transition between superconductive and normal conductive state was nonlinear (see

Figures 55 and 56). The measurements were generally compatible with the results gained with the smaller coil and the permanent magnet. Small differences occur, due to uncertainties in the determination of the interaction length in the measurements with the permanent magnets and the small test coil, since they had a circular cross section between HTS wire and magnetic field. Again one could neglect the influence of a parallel field, it had no measurable effect on the resistance of the wire.

This measurement showed that for a perpendicular field of 0.1 T the critical current I_C was about 60 A while for a field of 0.2 T the critical current was 30 A at LN_2 temperature.

3.2.5 Measurements in LAr

Using the same setup as before, the LN_2 (≈77 K) was exchanged by LAr (≈87 K). To save some LAr, liquid nitrogen was used to cool down the HTS wire and the connections to a temperature close to the boiling point of argon. The temperature of the HTS wire resistance was measured continuously for B=0 T and when the resistance for an applied current of 67 A was not measurable, the wire had to have a temperature below 95 K (see chapter 2.1). After reaching this temperature, the

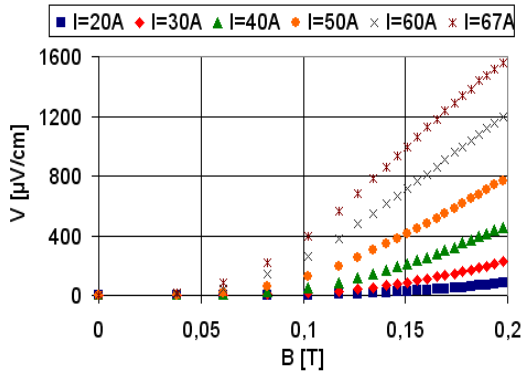

Figure 57: *Measured voltage drop per cm of HTS wire in LAr as a function of the perpendicular B-field for different currents.*

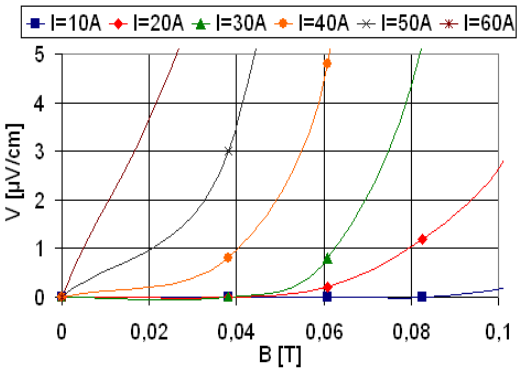

Figure 58: *Expanded view of Figure 57 for perpendicular magnetic fields up to 0.1 T in LAr.*

liquid argon was added. To reduce the heat input (e.g. slowing down the vaporization rate of the liquid argon) a box filled with liquid nitrogen was placed on top of the box containing the HTS wire and the coil, creating a thermal shield.

At first the perpendicular B-field was applied to the HTS wire. The resistance of the wire increased linearly after the transition from superconductivity to normal conduction, like in the measurements with LN_2 before. However, the resistance at LAr temperature was generally about a factor 20 higher than at LN_2 temperature (see Figures 58 and 57). A perpendicular magnetic field of 0.05 T had a critical current of 35 A, a field of 0.1 T had a critical current of about 10 A.

The setup was warmed up and the HTS wire was rotated to measure the influence of a parallel magnetic field. The described cooling procedure was again used and the liquid argon was added to the setup.

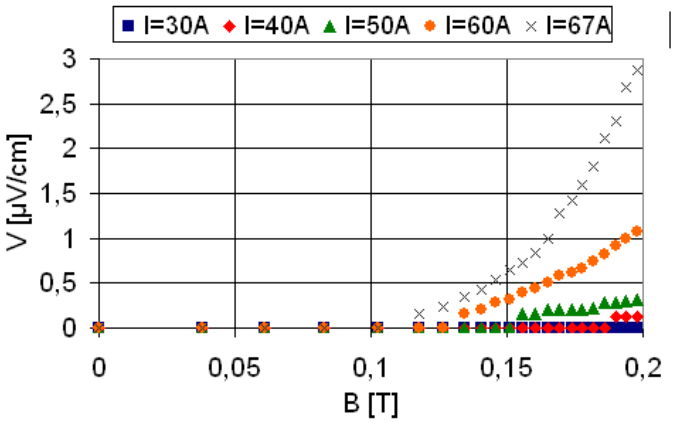

Figure 59: *Measured voltage drop per cm of HTS wire in LAr as a function of the parallel B-field for different currents.*

A parallel field of 0.2 T had a critical current of about I_C=60 A (see Figure 59). Comparing the measurement with the result of chapter 2.1, the critical current was higher than estimated. This is due to the fact that the data sheet only gave information about the minimal guaranteed critical currents, i.e. higher currents than 45 A could possibly be applied to the wire.

Contrary to the measurements at liquid nitrogen temperature, both, parallel and perpendicular magnetic fields have a measurable effect on the critical current I_C. Already low perpendicular fields of 0.05 T will reduce the critical current to values below 40 A, while a parallel field of 0.2 T has a critical current of 60 A. Therefore, further simulations of the solenoid have to be made to reduce the perpendicular fields as much as possible.

3.3 Reopening the connection

During the changes in the setup between the measurement with the small test coil and the big test coil the HTS wire was damaged, a part of the wire was bent beyond the minimal bending radius. Hence, a new test wire had to be made, since for the damaged part of the HTS wire no superconductivity could be reached again. This shows the sensitivity of the HTS wire to bending, as a consequence more precaution had to be taken when handling the wire.

The copper block was reopened and the wire was again connected to the copper block like it was explained in chapter 3. Again the resistance of the connection was measured, the resistance was 0.4 $\mu\Omega$, i.e. the same value as before was achieved. As

Figure 60: *Reopened copper block, the non uniform surface hints that the soldering was only partly successful.*

Figure 61: *Expanded view of the copper block surface, remains of the flux and not soldered areas are visible.*

seen in Figures 60 and 61 the reopened copper block showed that not the complete copper block surface was soldered. One can see remains of the flux and areas, where the indium solder did not connect both copper block halves. Nevertheless, the measurements indicate that these imperfections have little effect on the resistance of the connection, the connecting area between HTS wire and the copper block is still big enough.

4 Design of the solenoid

Layer winding or so called "pancakes" are the common solutions to design solenoids with HTS wires [99]. A pancake is a small coil consisting of several layers of single width HTS wire wound on top of each other. Several pancakes are then stacked on a mechanical support and connected with each other to build up the coil, while for layer winding a single continuous wire is wound for the whole coil. Shorter HTS wires used for pancakes are cheaper and quicker available than a single long HTS wire used for a layer winding, due to the wire fabrication process[4]. Another advantage of the pancake design is the possibility to increase the coil length by adding new pancakes to the existing setup, while layer winding uses a fixed length that can not easily be increased when the winding is finished. Therefore, a pancake design was chosen and further simulations were made using the program Elefant2D introduced in chapter 2.3. Since the solenoid still had to fit into the LAr dewar, the constraints to the solenoid geometry from chapter 2.3 had to be used to find a new solenoid geometry. Winding the HTS wire to a coil needs a coil support made of non-magnetic material; assuming a thickness of 2 mm for this support structure, the HTS wire layer had a minimal inner radius of 10.7 cm.

Since the HTS wire had a thickness of 0.39 mm, a pancake with 30 layers would have an outer radius of 11.9 cm, leaving 6 mm space between the coil and the inner dewar wall, which could be used for reinforcing elements and parts of the yoke. A full metal yoke was not applicable because it would be too heavy. Since the setup of the LAr TPC included the normal conducting SINDRUM-I magnet (see Figures 28, 31 and [6]), there was the possibility to use the SINDRUM-I yoke for the HTS solenoid too, simulations regarding this were made.

A pancake with an inner radius of 10.7 cm and an outer radius of 11.9 cm requires 21.5 m of HTS wire. An extra HTS wire with a (total) length of 1.5 m is needed to connect the pancakes with each other and to the normal conducting cables from the power supply. Several wire lengths (approximately 500 m, 800 m and 1000 m) were considered: a solenoid made out of 23 pancakes needs 496 m of HTS wire, a solenoid made of 37 pancakes needs 797 m of HTS wire while 47 pancakes need 1012 m of HTS wire.

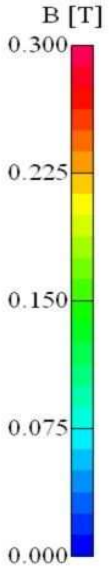

Figure 62: *Color code for the magnetic field strength used for the simulations presented in this chapter.*

[4]Hermetic HTS wire with a critical current of 145 A (for B=0 T) costs $32.30 per meter when delivered in pieces shorter than 100 m.

From the measurements presented in chapter 3.2.5 the effect of magnetic fields on the HTS wire at liquid argon temperature for different currents is known. The measurement of the parallel field indicates that the critical current I_C for a parallel field of 0.2 T was about 60 A (see Figure 59). For a current of I=60 A the maximal perpendicular magnetic field strength the HTS wire can be exposed to is less than 5 mT. This is a strong constraint for the design, therefore the maximal current for the simulation was restricted to a current of 50 A to ease the constraints on the perpendicular field to stay below 1 μV/cm (see Figure 58), i.e. small perpendicular B-fields up to 20 mT are affordable.

To present the results and compare the different simulations a uniform color code was used (see Figure 62). Due to the chosen scale magnetic fields above 0.3 T will be shown as white. If this case occurs, it will briefly be discussed.

4.1 Simulation of several solenoids with different wire lengths

The simulations were done for the geometries described above and for a current of I=50 A. If the symmetry of the problem is taken into account, the simulation can be limited to a fourth of the solenoid.

4.1.1 Coil with 500m of HTS wire

Implementing the 11.5 pancake coils for the solenoid version with about 500m of HTS wire without a yoke showed a very inhomogeneous magnetic field with an on-axis magnetic field of 0.07 T in the center. Adding mirror plates to the simulation and the iron yoke from the SINDRUM-I solenoid, used in the LAr TPC setup, created a homogeneous field of 0.07 T over the whole chamber area (see Figure 63).

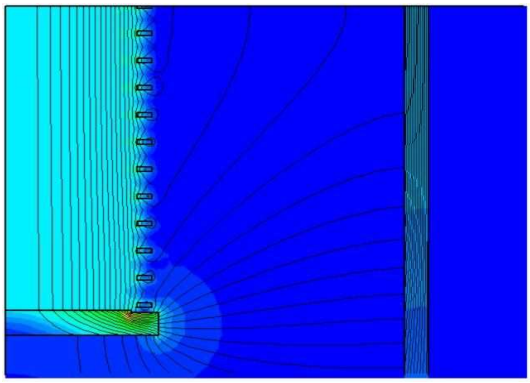

Figure 63: *2D simulation of the magnetic field for 23 unshielded pancakes with mirror plates and SINDRUM-I yoke.*

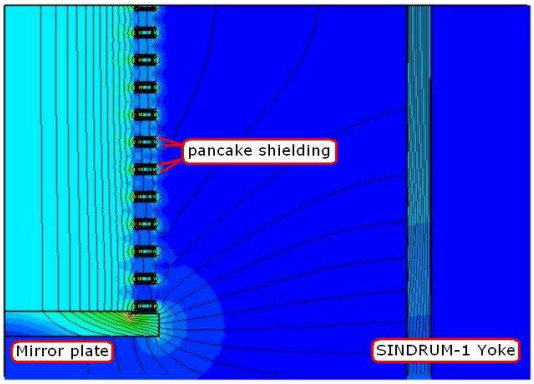

Figure 64: *2D simulation of the magnetic field for 23 shielded pancakes with mirror plates and SINDRUM-I yoke.*

Unfortunately, perpendicular magnetic fields occurring at the pancakes were so high that the critical current was zero. To reduce the perpendicular fields each pancake coil was shielded with a 2mm thick iron rings on both sides (see chapter 5.1) expanding over the inner and outer radius of the HTS wire winding (see Figure 64). This decreased the perpendicular fields of the pancakes enough. Although the parallel fields were increased by the iron rings, the critical current was not decreased below 50 A, providing an on-axis magnetic field of 0.07 T. With a variable distance

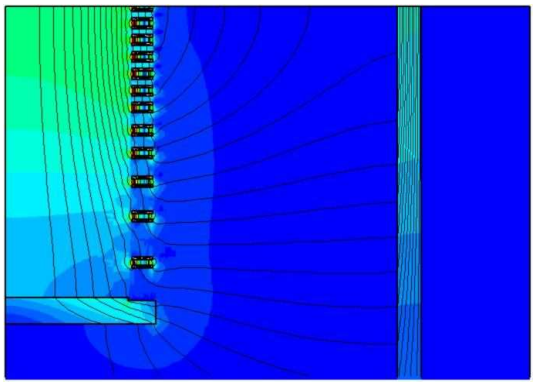

Figure 65: *2D simulation of the magnetic field for 23 shielded pancakes with mirror plates and SINDRUM-I yoke for varying distances between the pancakes.*

between the individual pancake coils an inhomogeneous field up to 0.1 T in the center of the magnet could be generated. The smaller the distance between the inner coils was, the higher was the magnetic field in the center of the solenoid (see Figure 65). Since the LAr TPC was situated in the middle of the solenoid with surrounding structures like the read-out this inhomogeneous field distribution was of use, since a higher central field would be generated where the drift volume was situated. Still, the estimated magnetic field strength of 0.1 T was less than aimed for.

4.1.2 Maximizing the B-field for a coil with 500m of HTS wire

The aim was to generate a field as high as possible. Two options existed to increase the field, either the wire length could be increased or the drift volume had to be reduced. Since the existing TPC was too big to be applied without changes to the solenoid it had to be re-engineered anyway. The readout plane could not be resized without building a completely new TPC, but the layout of the field shapers and the cathode could be changed without any bigger problems. To fit into the solenoid the width of the TPC had to be reduced by 5 cm, since the height of the chamber could not be changed. Therefore, the maximal drift length would be 10 cm instead of 15 cm.

Changes in the length of the drift volume can easily be made by reducing the number of field shaping electrodes and changing their layout. To use the 500 m wire

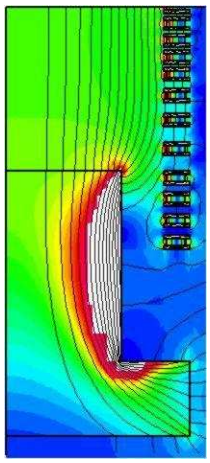

Figure 66: *2D simulation of the B-field for 23 shielded pancakes; I=50 A.*

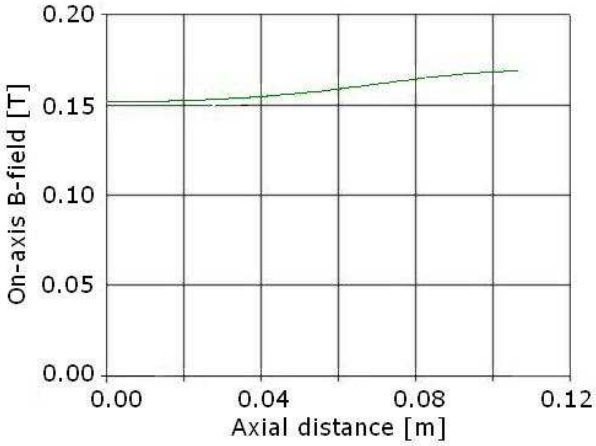

Figure 67: *On-axis B-field (from the center of the coil to the nose of the mirror plate of Figure 66) for 23 shielded pancakes.*

length, the drift volume was therefore hypothetically reduced from the actual size of $30 \times 15 \times 15$ cm^3 to $20 \times 10 \times 15$ cm^3 (length $\times$ width $\times$ height of the drift volume). The volume outside the drift volume in the center of the solenoid was supposed to contain iron, i.e. the flat mirror plate was modified with a 'nose' (see Figure 66). One can see that this setup had an on-axis magnetic field of 0.17 T for a current of I=50 A. Thanks to the iron nose, the whole drift volume had a very homogeneous magnetic field of about 0.15 T. The thermal input produced by the HTS solenoid was estimated to be 2-3 W.

4.1.3 Coil with 800m of HTS wire

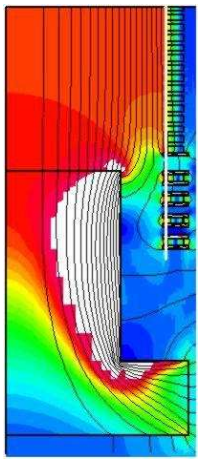

Figure 68: *2D simulation of the B-field for 37 shielded pancakes; I=50 A.*

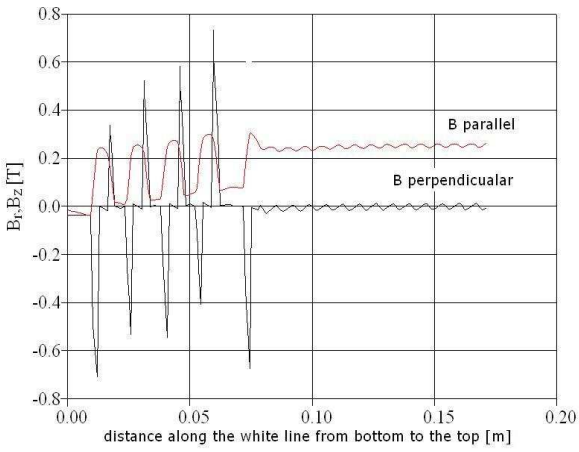

Figure 69: *B-field along the white line from Figure 68 from bottom to top. The peaks correspond to the location of the shielding rings.*

An even smaller drift volume than discussed in the previous section to gain a higher field was not considered, thus a longer HTS wire was assumed by increasing the number of the pancake coils. There are several possibilities to produce a higher magnetic field in the center of the solenoid. One way is to use all pancakes to magnetize the nose of the yoke and use the field between the two mirror plates with noses. The other possibility is to do the opposite, and apply the pancakes only to the drift volume, or to distribute the pancakes over the drift volume and the nose.

The simulations showed that the best way to obtain a high and homogenous field is to distribute the pancakes over the mirror plate and the drift volume.

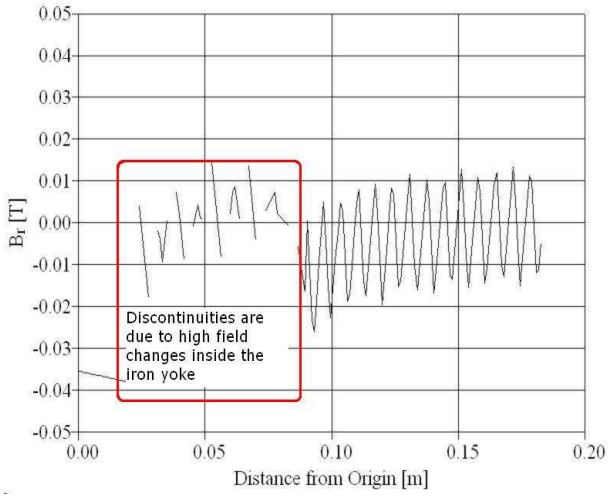

Figure 70: *Expanded view of the perpendicular B-field along the white line from Figure 68 for 37 shielded pancakes using a modified TPC volume of* $22 \times 10 \times 15\ cm^3$.

Optimizing the pancake distribution (see Figure 68) showed that an on-axis B-field of 0.25 T could be generated for I=50 A per turn. The white line in Figure 68 represents a path along the inner surface of the pancakes, the parallel and perpendicular fields, shown in Figure 69 (from the outside to the inside of the solenoid). The occurring perpendicular magnetic fields applied to the inner surfaces of the pancakes (and therefore the HTS wire) were below 0.02 T as shown in detail in Figure 70, while the parallel magnetic field was 0.25 T for the applied current of 50 A. Thus, neither the parallel nor the perpendicular magnetic fields constrained the critical current I_C below 50 A. The thermal input produced by the HTS solenoid was estimated to be about 5 W.

4.1.4 Coil with 1000m of HTS wire

Adding further pancakes increases the wire length to about 1000 m. The simulations show that a number of 47 pancakes generate a magnetic field of 0.33 T assuming the reduced drift volume and a current of I=50 A. Although this sounds promising, this

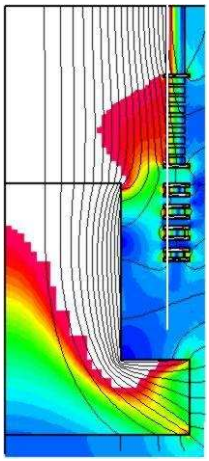

Figure 71: *2D simulation of the B-field for 47 shielded pancakes; I=50 A.*

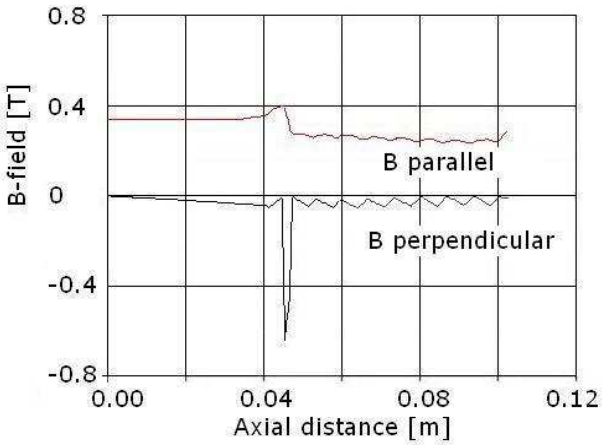

Figure 72: *B-field along the white line in Figure 71 for 47 shielded pancakes using a modified TPC volume of* $22 \times 10 \times 15$ cm^3.

result is not valid: the simulated parallel magnetic field of 0.33 T on the inner surface of the pancakes reduces the critical current I_C below 50 A and the perpendicular magnetic field at the pancakes was up to 0.1 T, decreasing the critical current I_C to zero (see Figures 71 and 72).

Therefore, an optimization of the shielding was done and the perpendicular fields decreased to a maximal value of 0.04 T. The critical current applicable was only 40 A, and the simulation was repeated with this current, instead of applying a current of 50 A. The result was that only a field of 0.25 T was generated on the axis, this is the same value reached with a 800 m HTS solenoid (see Figure 73). Also, the thermal input by the HTS solenoid was again about 5 W.

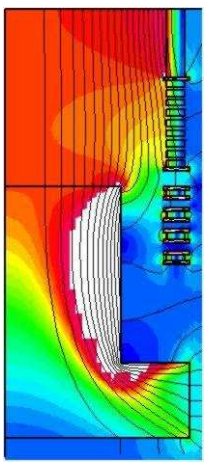

Figure 73: *2D simulation of the B-field for 47 shielded pancakes; I=40 A.*

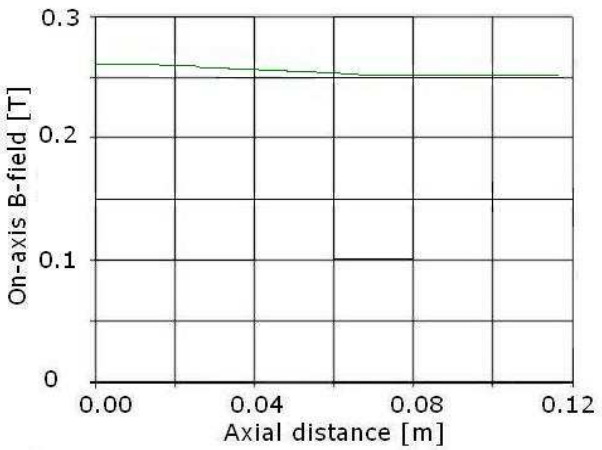

Figure 74: *On-axis B-field from the center of the coil to the nose of the mirror plate in Figure 73 for 47 shielded pancakes.*

Hence, an increase in the wire length for the reduced drift volume did not show an improvement of the magnetic field, due to the constraints occurring from the HTS wire performance, decreasing the critical current I_C. Further simulations showed that the drift volume could be increased while the produced magnetic field in the center was still about 0.25 T for a current of I=50 A; therefore, an increase in the HTS wire length did not generate higher magnetic fields but increased the possible drift volume.

4.2 Summary of the results

For an inner diameter of the coil of 21.4 cm B-fields between 0.1 T up to 0.25 T can be produced, depending on the wire length and the TPC volume as shown in Table 1. For a wire length of 1012 m two possibilities for the drift volume and therefore the critical current exist. For the assumed currents of the simulation also the estimated critical current is given from the measurement of chapter 3.2.5. Since a pancake design was chosen a step by step increase in the total wire length is possible when a suitable coil support is available.

Total HTS wire length	496 m	797 m	1012 m	1012 m
Number of Pancakes	23	37	47	47
Magnetic field on the axis	0.1 T*	0.25 T*	0.25 T*	0.25 T
Assumed current	50 A	50 A	40 A	50 A
Estimated critical current	60 A	50 A	40 A	50 A

Table 1: *Comparison of the solenoids made with different HTS wire lengths (*means a reduced drift volume of* $20 \times 10 \times 15$ *cm*^{3}*).*

5 Building a small test solenoid

5.1 Design of the test solenoid

Two 50m long pieces of HTS wire[5] were purchased from AMSC to build a small test solenoid for a proof of principle. Figure 75 shows schematically the design of the coil considering four pancakes and a magnetized cylindrical volume with a height of 5 cm.

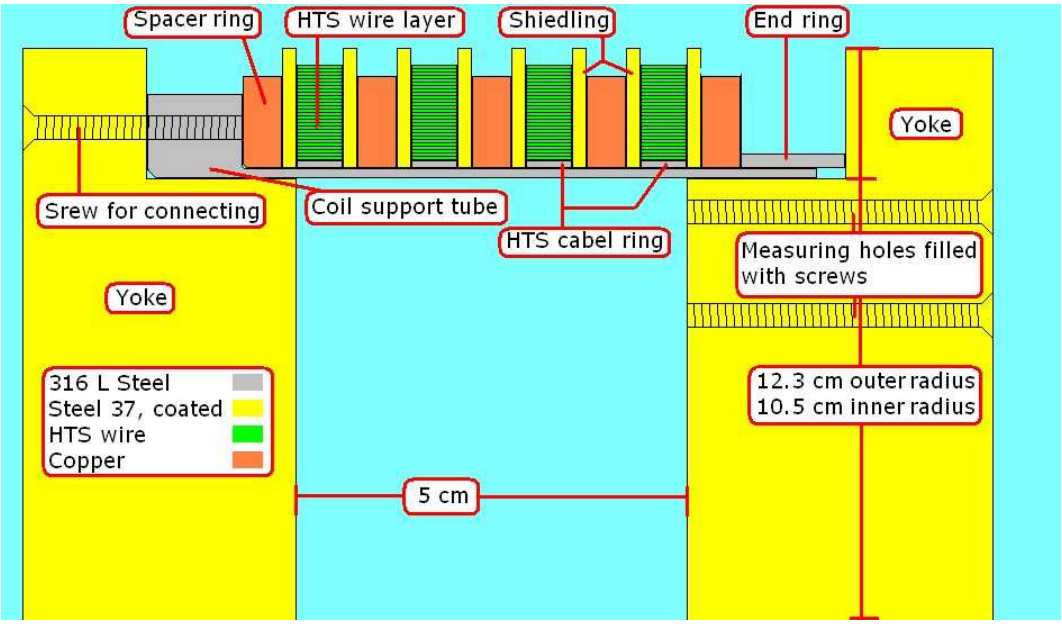

Figure 75: *Schematic view of the HTS solenoid showing the structural design for the coil support.*

Coil support: The coil support has to fulfil several needs. It has to be as thin as possible, but stable to withstand the occurring forces of the magnetic field. Also it has to have the possibility to support different wire lengths. A design with four shielded pancakes, covering 33 mm of the cylinder height of the coil volume, was chosen, alternating layers of HTS wire and spacer rings were assembled to build the coil and cover the TPC area. Therefore, a tube made of stainless steel 316L (non-magnetic) was chosen as core of the support structure, having an outer diameter of 213 mm and a thickness of 2 mm and a length of 70 mm. One end of the coil support had flange to be connected to one of the mirror plates, while the other side was open, thus, smaller rings could be mounted, i.e. spacer rings, shielding rings, and cable rings (the functions of these rings are explained later).

[5]Hermetic HTS wire with an average current density of 8500 A/cm and I_C=145 A.

Spacer rings: The spacer rings were made out of copper; they were 5 mm thick and had an inner diameter of 213 mm and an outer diameter of 240 mm. They were needed to cover a bigger volume and had a cut-out opening of 18mm width, seen in Figure 76, to connect the pancakes with HTS wire and the power supply.

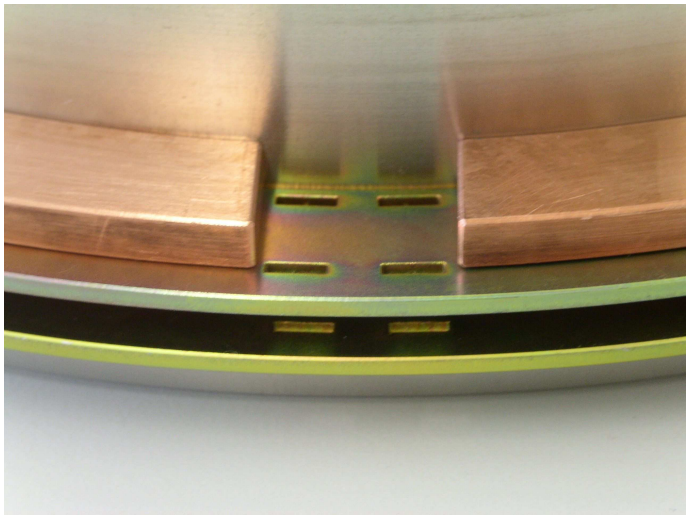

Figure 76: *Picture of the HTS solenoid structural design showing a shielding ring with a spacer ring completing a pancake segment.*

Shielding rings: Each pancake had to be magnetically shielded to reduce the perpendicular magnetic fields with a shielding ring made out of coated steel 37. A coating for the yoke parts, i.e. the shielding ring and the mirror plates was necessary, since during the warm-up of the solenoid in air a lot of water will condense on all surfaces. Without coating the steel 37 would oxidize, and later on the rust could contaminate the purified liquid argon of the TPC. A yellow zinc coating was applied, creating a good protection against corrosion. The shielding rings were 2 mm thick and had an inner diameter of 213 mm and an outer diameter of 240mm; four slits with a size of 5 x 1 mm^2, two at the inner and two at the outer radius (see Figure 76). The two connections were used for redundancy: if one would fail, the second one could still transport the current.

Cable Rings: Each pancake itself consisted of a cable ring made out of steel 316L, as shown in Figure 77. They had an inner diameter of 213.1 mm, a thickness of 2 mm and a width of 4.3 mm. The HTS wire was wound on this ring to a thickness of 1.2 cm corresponding to 30 layers of HTS wire (thickness 0.4 mm×30=1.2 cm), each layer separated to the other with a 70 μm polyester foil (not shown).

Total number of rings: Altogether there were 8 shielding rings, 4 cable rings and 5spacer rings needed to build the solenoid. An end ring made out of steel 316L

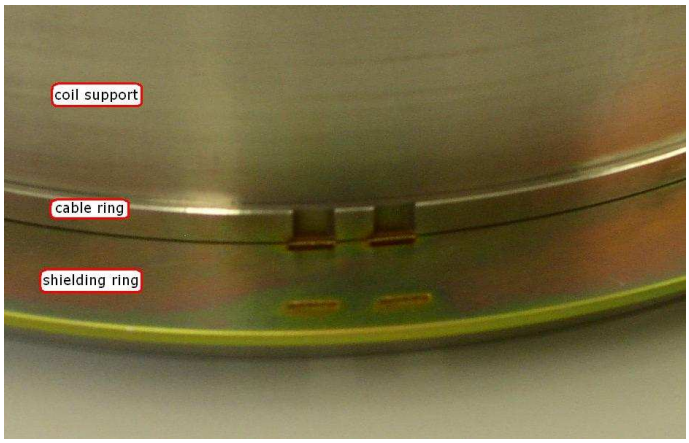

Figure 77: *Picture of the HTS solenoid structural design showing a shielding ring with a cable ring.*

with an inner diameter of 213.1 mm, a thickness of 3 mm and a length of 10 mm was used to hold the structure together.

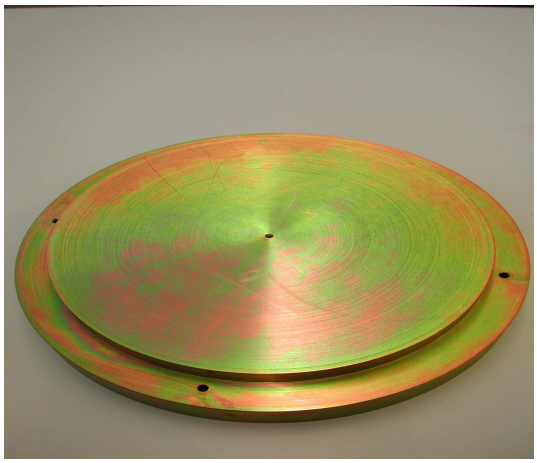

Figure 78: *Picture of the mirror plate, 4 screws where used to connect it with the coil support.*

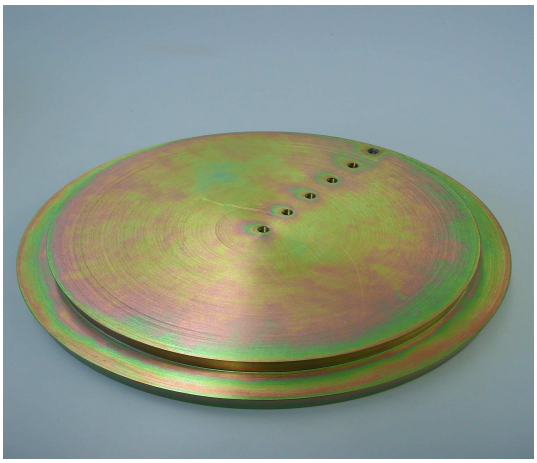

Figure 79: *Picture of the upper mirror plate, showing the screw-holes for the hall probe.*

Mirror plates: The yoke mirror plates were made out of massive steel 37 and coated with yellow zinc. One of the mirror plates was connected to the coil support with M4 screws (see Figures 75 and 78), while the other one had no screws. This was due to the fact that the test coil was standing vertically on the screwed mirror plate and the other end plate was lying on top of the coil support, using its weight to press the structure tightly together, so that no extra mechanical connection was needed. In the top end-plate were 6 radially aligned threaded holes with a distance of 2 cm between the holes (see Figure 79). Through these holes the Hall probe could

be inserted to measure the (axial) magnetic field inside the coil; the holes not used for the probe were filled with a screw.

5.2 Calibration of the Hall probe at low temperatures

Magnetic fields are most commonly measured with Hall probes. The Hall effect, which is used for the measurement of the magnetic field, depends on the mobility of the charge carriers in a semiconductor (or conductor). This mobility is temperature dependent and since the available Hall probes were only calibrated for room temperature (approx. 300 K), they had to be calibrated for LN_2 (77 K) and LAr (87.5 K) temperature. There were two available Gauss-meters, so first a comparison between the digital Bell 4048 and the analog Bell 610 Gauss-meter was made at room temperature.

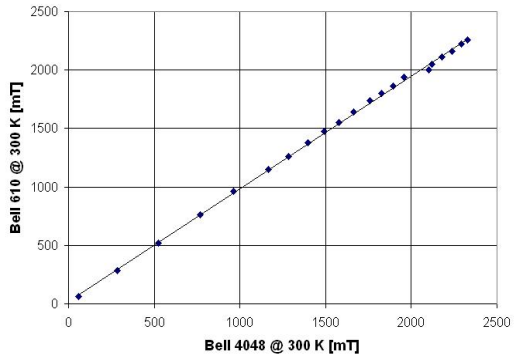

Figure 80: *Comparison of the B-field measured with the Bell 4048 and the Bell 610 Gauss-meters.*

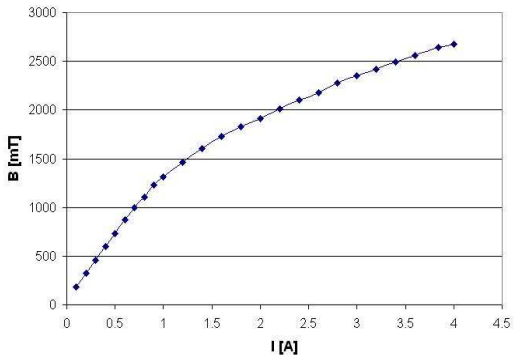

Figure 81: *Magnetic Field produced by a small electromagnet for the calibration of the Hall probe.*

Both Hall probes measure nearly the same magnetic field, small differences occur when the measurement range is changed (see Figure 80). Only the Bell 610 was used for measurements in the liquid gases since the Bell 4048 is a handhold instrument developed for room temperatures, having a Hall sensor plus a cable with a length of 4 cm only; thus, for an application in liquid gases the whole instrument had to be cooled, which is impossible since its digital display only works at room temperature. The Bell 610 on the other hand can be used.

To calibrate the Bell 610 Gauss-meter the following setup was used: An electromagnet was used to produce a magnetic field, which was measured first at room temperature. Depending on the applied current the magnetic field of the electromagnet could be varied (see Figure 81). The Hall probe was situated in a small dewar, which could be filled with liquid nitrogen or argon (for a non-filled dewar the temperature was the room temperature). The measurements the magnetic field measured at the temperature of the liquid gases was compared to the measurement at room temperature.

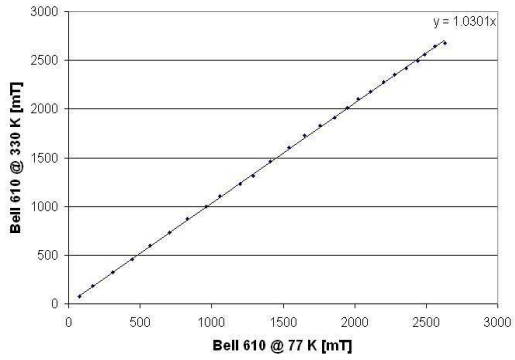

Figure 82: *Comparison between the magnetic field measured with the Bell 610 Gauss-meter at room temperature and LN_2 temperature.*

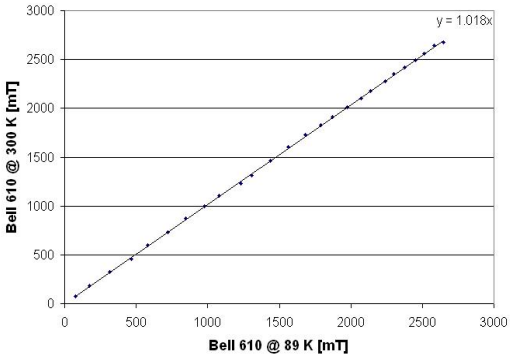

Figure 83: *Comparison between the magnetic field measured with the Bell 610 Gauss-meter at room temperature and LAr temperature.*

There were differences of 5 mT between the measurement at 77 K and 300 K, for 89 K the difference was only about 3.5 mT (see Figures 82 and 83) for a field of B=0.26 T. A linear fit was made to evaluate the magnetic field from the measurement at low temperatures: for LN_2 the magnetic field can be calculated as $B_{real} = 1.0301 * B_{measured}$, and for LAr the magnetic field can be calculated as $B_{real} = 1.018 * B_{measured}$. If in the following chapters any measurement of magnetic fields is mentioned, the results will be given in the calculated room temperature equivalent.

5.3 Mounting the solenoid and first tests

5.3.1 Winding a pancake

To wind the pancakes, the coil was mounted with two aluminum end plates on a lathe. When the lathe was rotating slowly, the HTS wire and the insulation tape were wound together on the cable ring, as shown in figure 84. The space in between the shielding rings in which the HTS wire and the insulation were wound was very tight; it had the same width as the HTS wire and the tape. HTS wires do not necessarily need insulation between the layers, since the current will only be transported in the superconductive wire parts, but since the exposure to magnetic fields causes the superconductivity to breakdown, an insulation was added to avoid leakage currents.

Figure 84: *Picture of the winding process on a lathe. The HTS wire coming from the right is insulated with the yellow tape.*

5.3.2 Connecting the pancakes

When building the coil out of individual pancakes one has to be careful that the current always circulates in the same direction. The pancakes are alternating connected at the inner or at the outer radius to the next one, so that each pair of adjacent pancakes consists of one pancake that is wound clockwise while the other one is wound counterclockwise. Although several tests to splice the HTS wire to normal conducting wires were made (see chapter 3), the pancake design required additional splicing tests, since this time the HTS wires had to be spliced with each other. The two connecting wire pieces (2 cm long each) were soldered at a right angle to the windings, as shown in Figure 85.

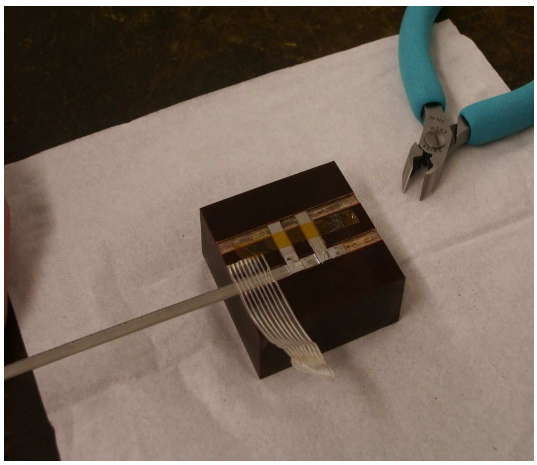

Figure 85: *Picture of plastic holder on which the HTS wire crossover was soldered.*

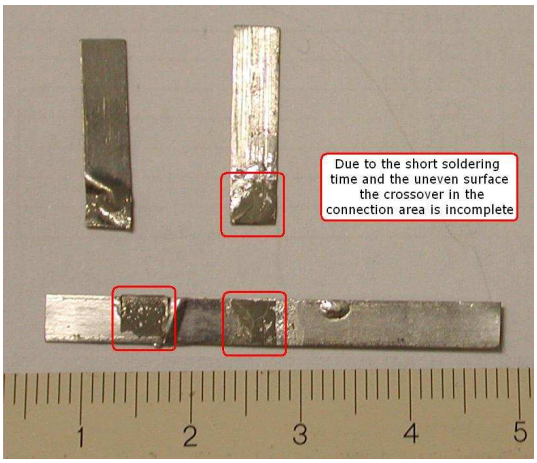

Figure 86: *Reopened connection of spliced HTS wires for the pancake connection.*

Therefore, the connecting area had a size of twice 4.3 x 4.3 mm^2, through which the current had to pass from one HTS wire to the other one through the matrix of the wires. The first test was simply to solder the wires with a big soldering gun. The result is shown in Figure 86. The resistance of such a connection was $0.63 \pm 0.08\,\mu\Omega$.

Further improvements were achieved when also a resin flux was used. Since the connections had to withstand thermal and mechanical stress, two connections were made; if one failed, the other could transport the current, and if both were okay, the resistance adds in parallel. The most important issue was to keep the soldering time as short as possible, since else the hermetic insulation of the HTS wire was damaged. Although it does not destroy the HTS layer of the wire, it could destabilize the wire structure by the ballooning effect described in chapter 1.3.5.

5.3.3 Test measurement with two pancakes and comparison with magnetic field calculations

To test the connection between the pancakes, at first only two pancakes were finished and connected to the power supply. Due to a misplaced HTS wire feed-through only 24, respectively 23 layers could be wound for the first pair of pancakes instead of the planned 30 layers.

The two pancakes were connected with the power supply and cooled down to 77 K and the produced magnetic field was measured. To test the consistency between the results of the measurement and the theoretical prediction of the 2D simulation with the software 'elefant2d', a simulation of these two pancakes was made, shown in Figure 87.

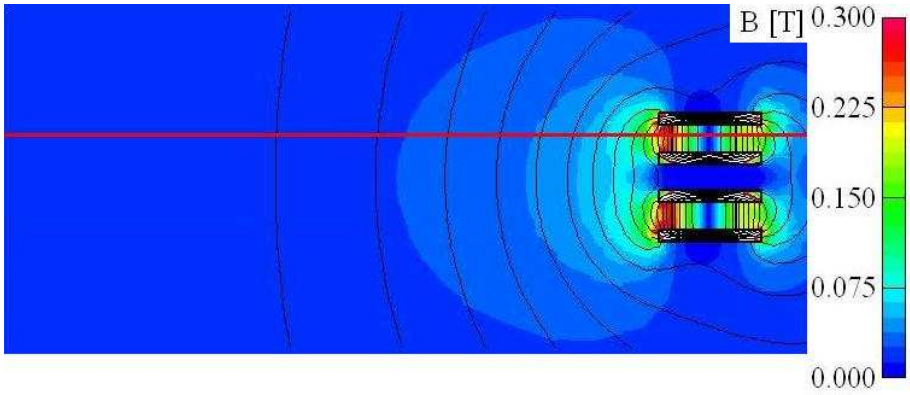

Figure 87: *2D simulation of the magnetic field produced with 2 pancakes (23 and 24 layers) for a current of I=68 A. The inner radius is 10.7 cm, the gap between the pancakes is 5 mm.*

Since the mirror plates were not available at this time, the measurement and simulation were made without them. Applying a current of 68 A a magnetic field

of 0.1 T was measured at the inner wall of the coil support, and a magnetic field of 0.02 T was measured in the center of the magnet. There was no way to measure directly the magnetic field at the innermost layer of the pancake, only about 4 mm away at the inner wall of the coil support is a measurement possible.

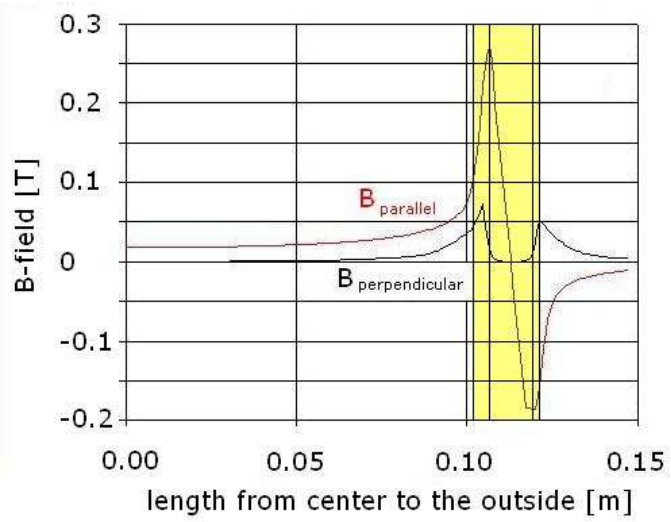

Figure 88: *B-field along the red line in Figure 87 for 2 pancakes (23 and 24 layers) for a current of I=68 A. The radial extension of the coil is marked yellow, indicating 3 layers, the inner coil support, the HTS layer and to the outside the outer part of the shielding rings.*

The simulation predicts a field of about 0.1 T at that point, i.e. the simulation and the measurements agree (see Figure 88). The two pancakes with a HTS wire length of about 40 m and the connections between them had a voltage drop ('resistivity') of 2 μV at a current of 4 A for a temperature of 77 K, and for a current of 68 A the voltage drop ('resistivity') was 3 μV, i.e. the whole HTS wire seems to be still superconductive. No test was made in LAr.

5.4 2D simulation of the magnetic field for 4 pancakes

After winding the last 2 pancakes, the mounting of the test solenoid was finished. To compare the results with the measurement, again a 2D simulation was made. The two new mounted pancakes had 28 respectively 27 windings. The mirror plates were also available at this time, so that the simulation was made for 4 pancakes with 23, 24, 28 and 27 layers and mirror plates. The result, as seen in Figure 89, shows a homogeneous magnetic field of 0.1 T inside the solenoid for a current of 66 A.

The magnetic field components reaching a value of 0.25 T for the innermost layer of the solenoid is shown in Figure 90 (along the white line of Figure 89). Since the

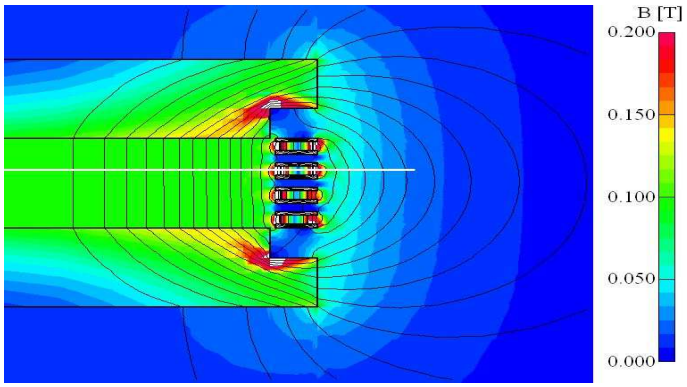

Figure 89: *2D simulation of the magnetic field produced with 4 pancakes (23, 24, 28 and 27 layers) for a current of I=66 A.*

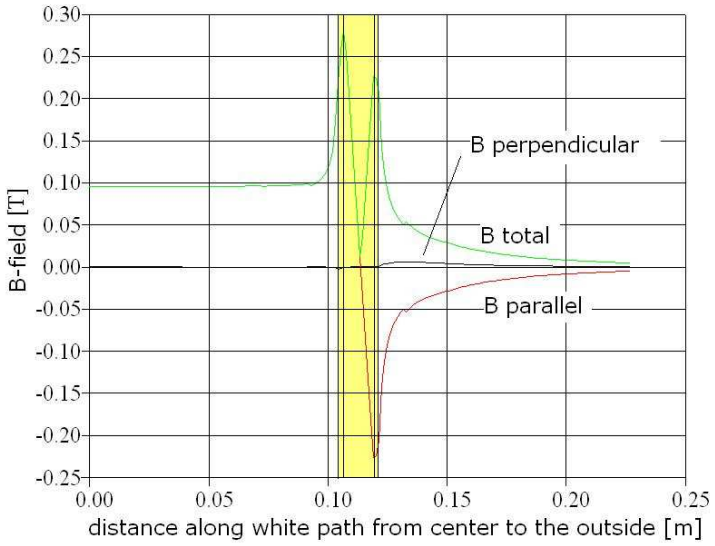

Figure 90: *B-field components along the white line in Figure 89 for 4 pancakes (23, 24, 28 and 27 layers) for a current of I=68 A. The radial extension of the coil is marked yellow, indicating 3 layers, the inner coil support, the HTS layer and to the outside the outer part of the shielding rings.*

perpendicular field does not exceed 0.02 T, the estimated current of 50 A in liquid argon (see chapter 4) is expected to be applicable without any problems.

5.5 The used power supplies

To test the coil two power supplies were used. One was called Mk2, built by Oxford Instruments, having an maximal current of 68 A[6], the other one was a HP Agilent 6453A with an maximal current output of 200 A[7]. The HP power supply was an old device and the current could not be measured reliable with the built-in amperemeter; a loop current transducer, the LEM HAL 200-S, was used to measure the current. The output voltage of this transducer was equivalent to the current (1 V $\approx$ 50 A).

Since the load of the power supply was a coil with an inductance the ripple of the power supply had to be as low as possible to measure the resistance, since else the induced voltage could destroy the measurement. Therefore, first the inductance of the coil was measured with the Escort ELD-3131D, a RLC-meter. For two test frequencies of 120 Hz and 1 kHz the inductance was measured to be about 0.5 mH. Afterwards the coil was cooled with liquid nitrogen and for both power supplies the ripple was measured for different currents. This was done with the Tektronix TDS 744A oscilloscope, which had a 3.5" floppy drive to transfer the data to a PC.

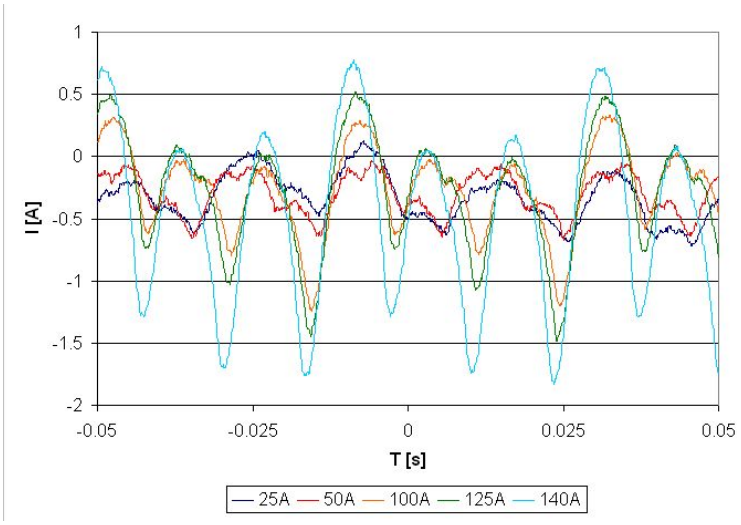

Figure 91: *Ripple of the HG Agilent 6453A power supply for different currents.*

The first test with the HP Agilent 6453A showed a main component of the ripple of about 3 A (peak to peak) for an output current of 140 A, and about 0.5 A for a current of 25 A, as shown in Figure 91, changing with a period of 25 Hz. In addition, there are two smaller peaks, due to the 3-phase AC current applied to the power supply.

[6]We thank K. Mattenberger from the Institute for Solid State Physics of ETH for lending us the power supply.

[7]We thank M. Horvat from the SLS group of PSI Villingen for lending us the power supply.

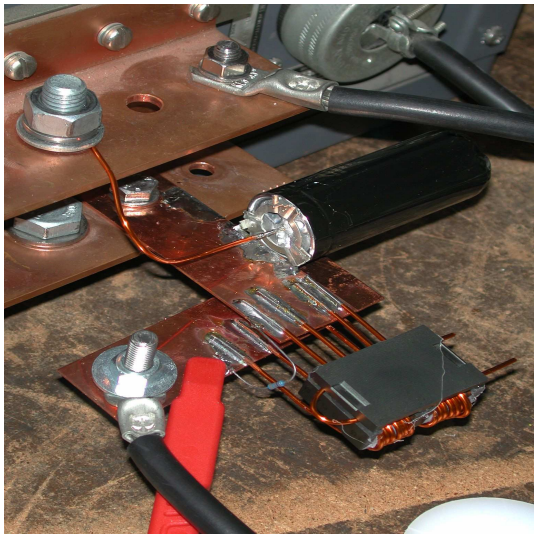

Figure 92: *Picture of the added capacity and coil.*

To stabilize the current a capacity of 200 F (maximal voltage 2.5 V) was added and an inductance of 0.5 μH, attenuated with a resistor of 1 Ω, shown in Figure 92. This reduced the ripple of the power supply by nearly a factor of 10 to 300 mA for a current of 145 A and 150 mA for a current of 10 A, changing with a period of 50 Hz and showing less influence of the 3-phase AC current (see Figure 93).

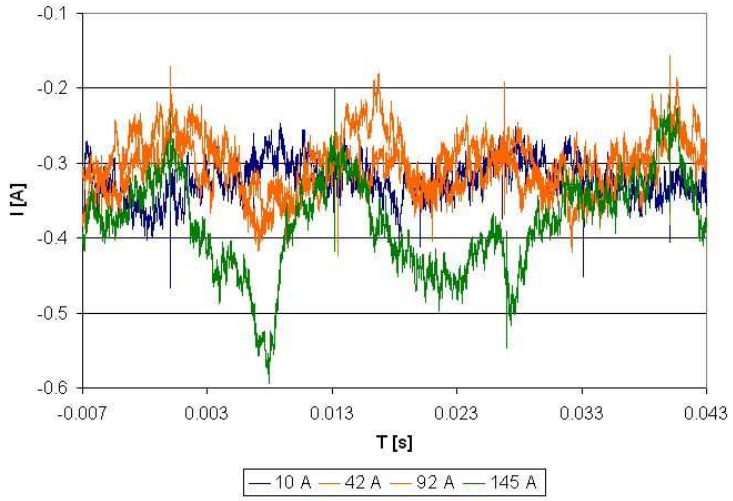

Figure 93: *Ripple of the stabilized HG Agilent 6453A power supply for different currents.*

The 68 A power supply from Oxford Instruments had a ripple of only 100 mA, which did not increase with the current, changing with a frequency of 50 Hz, as shown in Figure 94.

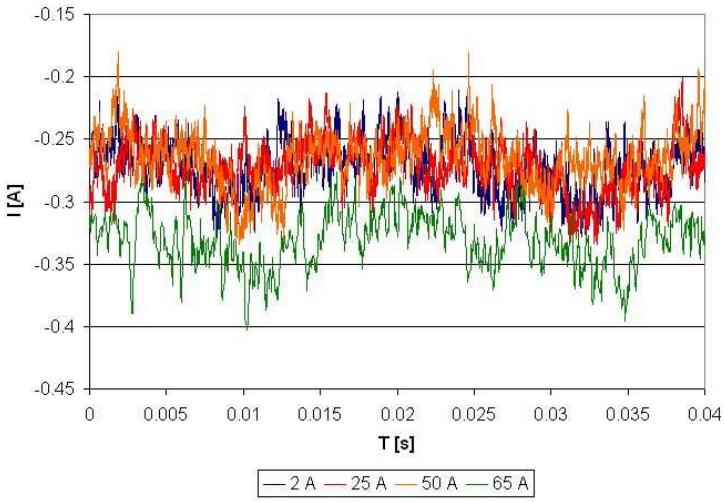

Figure 94: *Ripple of the Oxford Instruments Mk2 power supply for different currents.*

As a result of these measurements the Oxford Instruments Mk2 was used for small currents up to 66 A while the HP Agilent 6453A was used for higher currents. Only few measurements were made with the HP Agilent power supply for currents below 66 A to compare the results of both power supplies. Due to the higher ripple of the HP Agilent 6453A the measurement of the resistivity at low currents was barely possible, since the induced voltages were higher than the DC voltage drops of the coil resistance, i.e. instead of a voltage drop of some μV the value was oscillating between $\pm$ few mV, for higher currents this effect became negligible.

5.6 Results

The solenoid was tested in liquid nitrogen and liquid argon. The 4-point measurement was used again, to measure the resistance of the HTS coil (the method was already explained in chapter 3.1). The innermost HTS wire layer of the coil is exposed to a higher field than the other ones and the coil had a resistance due to the HTS wire connections of the pancakes. Thus, a result given as voltage drop per cm does not represent the reality. Thus, not the Voltage drop per cm, but the total resistance of the coil with a wire length of about 80 m will be given.

5.6.1 Resistance measurements

LN_2 : The resistance of the coil at LN_2 temperature for small currents is about 6 $\mu\Omega$, as shown in Figures 95 and 96. For currents higher than 40 Ampere it starts to raise and for a current of 70 A it is nearly doubled to 11 $\mu\Omega$; for 90 A it is already 28 $\mu\Omega$. For higher currents the resistance raises exponentially as seen in the logarithmical plot until a current of 145 A is reached, corresponding to the critical

current I_C from the data sheet. Increasing the current from 144 A to 145 A increases the resistance by a factor 2.

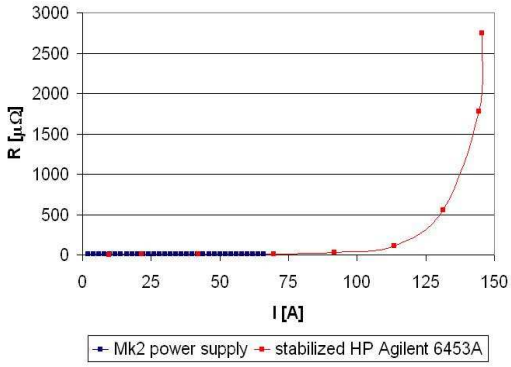

Figure 95: *Resistance of the solenoid in LN_2.*

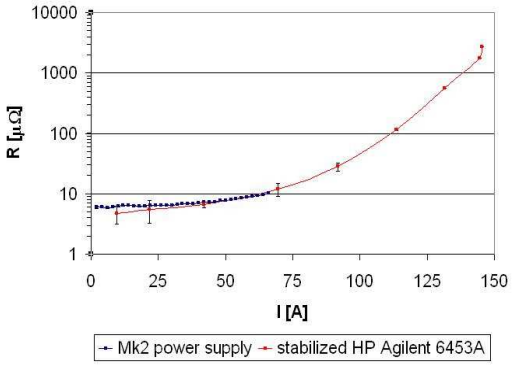

Figure 96: *Resistance of the solenoid in LN_2, logarithmical scale.*

LAr : A similar curve is obtained in LAr, as shown in Figures 97 and 98. For small currents the resistance of the coil is 6 $\mu\Omega$ and starts to raise for currents higher than 20 Ampere. For a current of 40 A it is nearly doubled to 11 $\mu\Omega$, for 55 A it is 32 $\mu\Omega$. For higher currents the resistance raises exponentially as seen in the logarithmical plot until a current of 80 A is reached. Increasing the current from 79 A to 80 A increases the resistance by a factor 2.

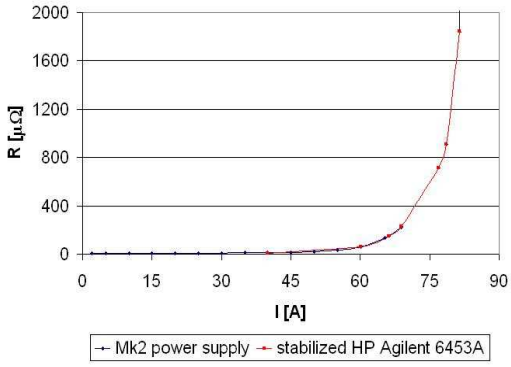

Figure 97: *Resistance of the solenoid in LAr.*

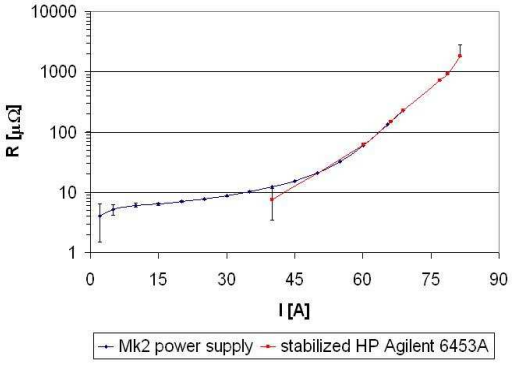

Figure 98: *Resistance of the solenoid in LAr, logarithmical scale.*

For both measurements higher currents than the currents of 145 A, respectively 80 A, could not be measured, since at that point the superconductivity of the HTS wire breaks down and the voltage and the current start to oscillate. To avoid damage to the coil and the damping capacity the power supply was therefore turned off.

5.6.2 Measurement of the magnetic field

The magnetic field was measured with the Bell 610 Gauss-meter via the holes in the top mirror plate. For the measurement 6 possible positions on the radius exist with a distance of 2 cm to each other. The field in the center was 20 mT lower than closer to the coil support, as expected from the simulation presented in Figure 90. To compare the magnetic field in LN_2 and LAr a measurement 2 cm away from the coil support, i.e. at a radius of 8.5 cm from the center of the solenoid was made for the parallel field. The perpendicular field was not measurable since no Hall probe sensitive to the perpendicular B-field inside the solenoid was available.

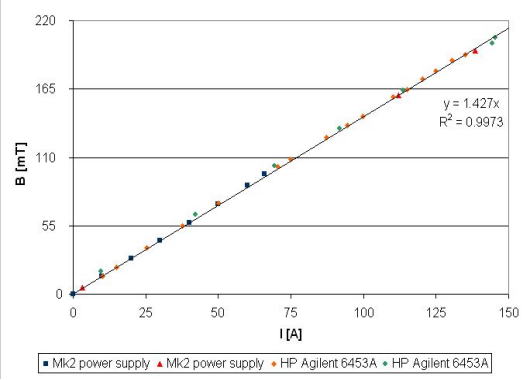

Figure 99: *Parallel B-field produced with the small solenoid in LN_2.*

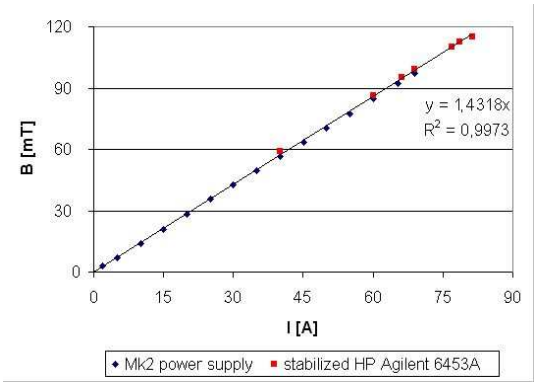

Figure 100: *Parallel B-field produced with the small solenoid in LAr.*

The produced parallel magnetic field raises linearly with the current, as shown in Figures 99 and 100. A maximum field of 0.2 T was reached in liquid nitrogen. For a current of 68 A the field strength was nearly 0.1 T, i.e. the measurement agrees with the theoretical prediction (compare with Figure 90). The linear dependence between current and magnetic field can be calculated as $B[mT] = I[A] * 1.43$.

5.7 Summary

The magnetic field produced by the small solenoid with only 4 pancakes (100 m of HTS wire) reaches a value of 0.11 T (I=80 A) at liquid argon temperature and 0.2 T (I=145 A) for liquid nitrogen. The critical current for liquid argon is about 80 A, while for liquid nitrogen 145 A is reached. The dependence of the resistance on the current is similar for both temperatures: if the current scale is stretched by a factor two for LAr the two curves coincide.

Cooling the setup in liquid nitrogen allows twice the magnetic field strength compared to argon, but no fields higher than 0.2 T can be achieved, since else superconductivity breaks down. The breakdown occurs at about a current of I=145 A, which is the critical current according to the data sheet for LN_2 temperature. Thus, the magnetic field of this coil is not the limiting factor of the current at LN_2 temperature.

At liquid argon temperature the estimated critical current of 97 A (see chapter 2.1) could not be applied, only a current of 80 A was possible, therefore, at LAr temperature the influence of the magnetic field is the limiting factor. As one can see from the measurements presented in chapter 3.2.5, the applied parallel magnetic field is limiting the current, the perpendicular field is irrelevant, since else the resistance should be much higher for low currents. Thus, the design of the coil, intended to reduce the perpendicular field at the HTS wire to below some 10^{-2} T, works like expected.

Temperature	LN_2 (77 K)	LAr (87 K)
Maximal applied current	145 A	80 A
On-axis B-Field	0.2 T	0.11 T
Coil resistance at 4 A	6 $\mu\Omega$	6 $\mu\Omega$
Resistance doubled at	70 A	40 A
Resistance quintupled at	90 A	55 A

Table 2: *Measurement results for the test solenoid at liquid nitrogen and liquid argon temperature.*

In the previous chapters the maximal possible current for the coil at liquid argon temperature was estimated to be 55 A to find an optimal balance between heat input and a magnetic field of 0.2 T. Since the prototype was limited to 4 pancakes with altogether 104 windings, a field of 0.2 T could not be produced in liquid argon. A a bigger prototype with more pancakes has to be built to test, whether 55 A is a good choice or not. For a field of 0.1 T a current up to 68 A can be applied without any problems due to heat input.

6 Summary & Conclusions

The feasibility to operate a coil made out of HTS wire in LAr was investigated in this thesis. First an extrapolation of the critical current I_C for the HTS wire from the AMSC data sheet was made up to liquid argon temperature. For no external B-Field the current is estimated to be about 100 A.

Afterwards first tests with external parallel and perpendicular magnetic fields, produced by permanent- and electro-magnets (up to 0.4 T, respectively 0.2 T) for an applied current up to 70 A were made, thus, determining the effect of these external fields on the HTS wire at LAr (=87 K) and LN_2 (=77 K) temperature. For a parallel B-field of 0.2 T the critical current in liquid argon is estimated to be about 60 A, while for a perpendicular B-field of 0.06 T the critical current is 30 A.

B-field	Estimated critical current	Measured critical current
0 T	100 A	$>$ 70 A
0.2 T (parallel)	50 A	60 A
0.06 T (perpendicular)	-	30 A

Table 3: *Estimated and measured critical currents for different B-fields.*

Next, two-dimensional simulations of the magnetic field for several solenoid structures (Helmholtz coil, single solenoid, single solenoid with a yoke) were made to evaluate the B-field components to which the HTS wire of a coil is exposed.

Three solenoids with different wire lengths were simulated, using the measurements of the effect of the external magnetic fields on the critical current of the HTS wire. A pancake coil design was chosen for HTS wire lengths of 500 m, 800 m and 1000 m. The parallel B-field was optimized by varying the distance between the individual pancakes and the magnetized volume. To reduce the influence of the perpendicular B-field the pancakes were shielded with a small iron ring.

Total HTS wire length	496 m	797 m	1012 m	1012 m
Number of Pancakes	23	37	47	47
Magnetic field on the axis	0.1 T*	0.25 T*	0.25 T*	0.25 T
Assumed current	50 A	50 A	40 A	50 A
Estimated critical current	60 A	50 A	40 A	50 A

Table 4: *Comparison of the solenoids made with different HTS wire lengths (*means a reduced drift volume of* $20 \times 10 \times 15$ *cm*^{3}*).*

Finally, a small prototype coil was built as proof of the concept, providing a quite homogenous B-field inside the volume with a B-field up to 0.2 T at LN_2 temperature on the axis, while exposing only very small perpendicular fields to the used hermetic HTS wire. For LAr temperature an on-axis B-field of 0.11 T was reached inside the

solenoid. The measured critical current at LN_2 temperature was about 145 A, equal to the value given on the data sheet. For LAr temperature the critical current was about 80 A (occurring from a parallel B-Field of 0.2 - 0.25 T to which the HTS wire was exposed to).

Temperature	LN_2 (77 K)	LAr (87 K)
Maximal applied current	145 A	80 A
On-axis B-Field	0.2 T	0.11 T
Coil resistance at 4 A	6 $\mu\Omega$	6 $\mu\Omega$
Resistance doubled at	70 A	40 A
Resistance quintupled at	90 A	55 A

Table 5: *Measurement results for the test solenoid at liquid nitrogen and liquid argon temperature.*

This results show the realistic possibility to build a solenoid with a B-field of 0.25 T at LAr temperature when using a high temperature superconductor wire.

Since in most cases the liquid argon volume is shielded with liquid nitrogen to avoid thermal losses, the coil could either be placed inside the argon or inside the nitrogen. For a better performance of the wire and higher fields the installation in liquid nitrogen is preferred since the magnetic field can be increased by a factor two.

7 Acknowledgement

I thank Prof. Dr. André Rubbia and Prof. Dr. Thomas Lohse for the opportunity to write my diploma thesis at the ETH Zürich. Special thank goes to Dr. Andreas Badertscher for his support and encouragement and his fair comments regarding my thesis.

Another thanks goes to Leo Knecht and Gusti Natterer for their aid in solving the technical problems; and of course Rosa Bächli from ETH Zürich and Prof. Rolf Köhler and Andrea Voigt from the examinations board of the HU–Berlin for their help in solving the administrative problems occurring with an external diploma thesis.

I also thank my family for their support during my time abroad, and of course many other people that eternising my stay abroad in Zürich. A special thank goes to Jasmin Zahn for her spell verification.

List of Figures

References

[1] ICARUS collaboration, http://www.aquila.infn.it/icarus/ and http://pcnometh4.cern.ch/

[2] CNGS collaboration, http://proj-cngs.web.cern.ch/proj-cngs/

[3] C. Rubbia, CERN-EP/77-08 (1977)

[4] Laboratori Nazionali del Gran Sasso, http://www.lngs.infn.it/

[5] The Particle Detector BriefBook http://rd11.web.cern.ch/RD11/rkb/titleD.html W. Blum and L. Rolandi, Particle Detection with Drift Chambers, Springer, 1993.

[6] M. Laffranchi, 'Small LAr TPC in a B-field' PhD thesis ETH No. 16002 (2005) A. Bardertscher *et al.* Nuclear Instruments and Methods in Physics Research A 555, p. 294 (2005)

[7] A. Ereditato and A. Rubbia, arXiv:hep-ph/0407297 (2004)

[8] S. Amerio *et al.* (ICARUS Collaboration), Nuclear Instruments and Methods in Physics Research A 527, p. 329 (2004)

[9] A. Bettini *et al.*, Nuclear Instruments and Methods in Physics Research A, 177 (1991)

[10] http://dept.physics.upenn.edu/balloon/cerenkov_radiation.html

[11] AMANDA collaboration, http://amanda.wisc.edu/

[12] ICECUBE collaboration, http://icecube.wisc.edu/

[13] ANTARES collaboration, http://antares.in2p3.fr/

[14] Fukuda S, et al. (Super-Kamiokande Collaboration), Physical Review Letters 81, p. 1562 (1998)
Fukuda S, et al. (Super-Kamiokande Collaboration), Physics Letters B 539, p. 179 (2002)
Y. Ashie *et al.* (Super-Kamiokande Collaboration), 'Evidence for an oscillatory signature in atmospheric neutrino oszillation', Physical Review Letters 93, p. 101801, (2004)

[15] CHOOZ collaboration, http://duphy4.physics.drexel.edu/chooz_pub/

[16] OPERA collaboration, http://operaweb.web.cern.ch/operaweb/index.shtml

[17] Davis, R., Progress in Particle and Nuclear Physics 32, pp. 13-32 (1994)

[18] A. Badertscher, M. Laffranchi, A. Meregaglia and A. Rubbia, New Journal of Physics 7, p. 63 (2005)

[19] A. Rubbia, arXiv:hep-ph/0402110 (2004)

[20] A. Rubbia, arXiv:hep-ph/0106088 (2001)

[21] A. Bueno, M. Campanelli, S. Navas-Concha and A. Rubbia, arXiv:hep-ph/0112297 (2002)

[22] D. B. Cline, F. Sergiampietri, J. G. Learned and K. McDonald, Nuclear Instruments and Methods in Physics Research A 503, p. 136 (2003)

[23] A. Rubbia, arXiv:hep-ph/0402110 (2004)

[24] S. Geer, arXiv:hep-ph/9712290 (1997)

[25] A. Ereditato and A. Rubbia, arXiv:hep-ph/0510131 (2004)

[26] A. Ereditato and A. Rubbia, arXiv:hep-ph/0409143 (2004)

[27] I. Gil-Botella and A.Rubbia, arXiv:hep-ph/0404151 (2004)

[28] Flare collaboration (Fermilab Liquid Argon Experiments), arXiv:hep-ph/0408121 (2004)

[29] A. Ereditato and A. Rubbia, arXiv:hep-ph/0509022 (2005)

[30] S Eidelmann *et al.*, Physics Letters B 592, eq. 27.10 (2004)

[31] GLACIER Project, http://neutrino.ethz.ch/GLACIER/

[32] Adapted from neutrino history by Didier Verkindt http://wwwlapp.in2p3.fr/neutrinos/aneut.html

[33] A. Becquerel, 'On the invisible rays emitted by phosphorescent bodies', Comptes Rendus 122, 501 (1896)

[34] E. Rutherford, 'Uranium Radiation and the Electrical Conduction Produced by it', Philosophical Magazine for January 1899, ser. 5, xlvii, pp. 109-163

[35] Mme. P. Curie, Comptes rendus de l'Académie des Sciences, vol. 126, p. 1101
P. Curie and Mme. P. Curie, Comptes rendus de l'Académie des Sciences, vol. 127, p. 175.
'On a New, Strongly Radio-active Substance Contained in Pitchblende' – P. Curie, Mme. P. Curie and G. Bmont (Translation of 'Sur une nouvelle substance fortement radio-active, contenue dans la pechblende') Comptes rendus de l'Académie des Sciences, Paris, 1898 (26 December), vol. 127, pp. 1215-1217.

[36] J. Chadwick, 'Possible Existence of a Neutron' in Nature, p. 312 (Feb. 27, 1932)
J. Chadwick, 'The Existence of a Neutron' in F.R.S. Proceedings of the Royal Society A 136, p. 692-708 (Received May 10, 1932)

[37] W. Pauli, in Rapports du Septime Conseil de Physique Solvay, Brussels, 1933 (Gauthier-Villars, Paris, 1934)

[38] F. Perrin, Comptes rendus de l'Académie des Sciences, vol. 197, p. 1625 (1933)

[39] Curie and Joliot, ' Comptes rendus de l'Académie des sciences,' vol. 194, p. 273 (1932)

[40] C. D. Anderson, Science 76, p. 238 (1932)
and 'The Positive Electron, Physical Review 43, pp. 491494 (1933)

[41] P. Dirac, Proceedings of the Royal Society A 117, p. 610 (1928)

[42] E. Fermi, Zeitschritf für Physik 88, p. 161 (1934)

[43] H. A. Bethe and R. Peierls, Nature 133, p. 532 (1934)

[44] B. Pontecorvo, National Research Council of Canada, Division of Atomic Energy. Chalk River, Report PD-205 (1946)

[45] F. Reines and C. L. Cowan Jr., Physical Review 90, p. 492 (1953)

[46] F. Reines and C. L. Cowan Jr., Physical Review 92, pp. 830831 (1953)

[47] C. L. Cowan Jr and F. Reines *et al.*, Science 103 (1956) and C. L. Cowan Jr. and F. Reines *et al.*, Physical Review 159 (1960)

[48] M. Schwartz, 'Feasibility of Using High-Energy Neutrinos to Study the Weak Interactions', Physical Review Letters 4, pp. 306307 (1960)

[49] J. W. Cronin, 'Studies of a Neon-Filled Spark Chamber',
Instrumentation for High-Energy Physics, Proceedings of an International Conference held 12-13 September, 1960 in Berkeley,
CA. Interscience Publications, p. 271 (1961)

[50] T. D. Lee and C. N. Yang, 'Theoretical Discussions on Possible High-Energy Neutrino Experiments', Physical Review Letters 4, pp. 307311 (1960)

[51] G. Danby and J. M. Gaillard *et al.*, Physical Review Letters 9, p. 36 (1962)

[52] S. L. Glashow, J. Iliopoulos, and L. Maiani, 'Weak Interactions with Lepton-Hadron Symmetry', Physical Review D 2, pp. 12851292 (1970)

[53] F. J. Hasert *et al.* (Gargamelle collaboration), 'Observation of neutrino like interactions without muon or electron in the Gargamelle neutrino experiment', Nuclear Physics B 73, p. 1 (1974) and Physical Letters B 46, pp. 138-140 (1973)

[54] A. Salam, 'Weak and electromagnetic interactions', (1969)
Proc. of the 8th Nobel Symposium on 'Elementary particle theory, relativistic groups and analyticity', Stockholm, Sweden, edited by N. Svartholm, p.367-377 (1968)

[55] S. L. Glashow, 'Partial symmetries of weak interactions', Nuclear Physics 22, pp. 579-588 (1961)

[56] S. Weinberg, 'A model of leptons', Physical Review Letters 19, pp. 1264-1266 (1967)

[57] M. L. Perl *et al.*, Physical Review Letters 35:, p. 1489 (1975)

[58] F. Abe *et al.* (CDF Collaboration), Physical Review Letters 73, p. 225 (1994)

[59] K. Kodama *et al.* (DONUT Collab.) Physical Letters B 504, p.218 (2001) and Nuclear Instrum. Methods A, 45 (2002)

[60] Scripts from P. Langacker, University of Pennsylvania Philadelphia available at http://dept.physics.upenn.edu/neutrino/ and informations found at Wikipedia http://de.wikipedia.org/wiki/Neutrinooszillation

[61] N. Schmitz, Neutrinophysik, Teubner Studienbücher, (1997)

[62] L. Wolfenstein, Physical Review D 17, p. 2369 (1978), Physical Review D 20, p. 2634 (1979)
S. P. Mikheyev and A. Yu. Smirnov, Yadernaya Fizika 42, p. 1441 (1985) [Sov. J. Nucl. Phys. 42, p. 913 (1985)]; Nuovo Cimento 9 C, p. 17 (1986)

[63] GALLEX collaboration, http://www.mpi-hd.mpg.de/nuastro/gallex.html

[64] SAGE collaboration, http://www.nu.to.infn.it/exp/all/sage/

[65] C. Athanassopoulos *et al.* (LSND collaboration), 'Evidence for neutrino oscillations from muon decay at rest', Physical Review C 54, p. 2685-2708 (1996) http://dnp.nscl.msu.edu/current/lsnd.html or http://www.nu.to.infn.it/exp/all/lsnd/

[66] M. H. Ahn *et al.* (K2K collaboration), Physical Review Letters 90, p. 041801 (2003)

[67] Q. R. Ahmed *et al.* (SNO Collab.), Physical Review Letters 89, p. 011302 (2002) http://www.sno.phy.queensu.ca/

[68] Das Mainzer Neutrinomassen-Experiment, http://www.physik.uni-mainz.de/exakt/neutrino/

[69] K. Eguki *et al.* (KamLAND collaboration), Physical Review Letters 90, p. 021802 (2003)

[70] W. W. M. Allison *et al.* (Soudan 2 collaboration), Physical Letters B, p. 137 (1999)

[71] A. Surdo *et al.* (MARCO collaboration), Nuclear Physics B Proceedings Supplement, 342 (2002)

[72] F. Boehm *et al.*, Physical Review D, 112001 (2001)

[73] Katrin Collaboration, http://wwwik.fzk.de/katrin

[74] T2K collaboration, http://neutrino.kek.jp/jhfnu/ and
http://neutrino.ethz.ch/T2K.htm

[75] List of Dark Matter experiments, http://neutrino.ethz.ch/ArDM/otherexp.html

[76] adapted from http://www.superconductors.org

[77] H. K. Onnes, Comm. Phys. Lab. Univ. Leiden, Nos. 119, 120, 122 (1911)
http://nobelprize.org/physics/laureates/1913/

[78] W. Meissner and R. Ochsenfeld, Naturwiss. 21, 787 (1933)

[79] Rutherford-Appleton Laboratory, http://www.cclrc.ac.uk/Activity/RAL/

[80] Fermilab, http://www.fnal.gov/

[81] V.L. Ginzburg and L.D. Landau, Zhurnal Eksperimental'noi i Teoreticheskoi Fiziki 20, p. 1064 (1950); Oxford: Pergamon Press, p. 546 (1965)
http://www.nobelprize.org/physics/laureates/2003/
http://de.wikipedia.org/wiki/Ginsburg-Landau-Theorie

[82] A. Abrikosov , Zhurnal Eksperimental'noi i Teoreticheskoi Fiziki 32, p. 1442 (1957) [Sov. Phys. JETP 5, p. 1174 (1957)]

[83] J. Bardeen, L. N. Cooper and J. R. Schrieffer, Physical Review 108, p. 1175 (1957)
http://www.nobelprize.org/physics/laureates/1972/

[84] B. D. Josephson, Physics Letters Volume 1, Issue 7 , p. 251-253 (1 July 1962)
http://www.nobelprize.org/physics/laureates/1973/

[85] K. Bechgaard, Physica B+C Volume 108, Issues 1-3, p. 1193-1194 (August-September 1981)

[86] W. A. Little, Physical Review A 134, p. 1416 (1964)

[87] J.G. Bednorz and K.A. Müller Zeitschrift für Physik B 64, p. 189 (1986)
http://www.nobelprize.org/physics/laureates/1987/

[88] A. Schilling, M. Cantoni, J. D. Guo, H. R. Ott, Nature 363, Issue 6424 , pp. 56-58 (1993)

[89] http://www.superconductors.org/type2.htm#record

[90] Vladimir Kresin, Physical Reports 288, p. 347 (1997)

[91] American Superconductor Corporation
http://www.amsuper.com

[92] MAGLEV collaboration
http://www.rtri.or.jp/rd/maglev/html/english/maglev_frame_E.html

[93] Splicing Information from email of
Ado Umezawa, AMSC Wire Buisness Unit

[94] Data Sheet of HTS – Hermetic Wire available at
http://www.amsuper.com/products/htsWire/documents/WFS_BHM_0705_r1.pdf

[95] Magnet Formulas Website by Eric Dennison
http://www.netdenizen.com/emagnet

[96] Institute for Fundamentals and Theory in Electrical Engineering
TU Graz (Austria)
http://www.igte.tugraz.at/index_en.html

[97] Article on the website of American Superconductor Corporation available at
http://www.amsuper.com/products/htsWire/103885178451.cfm

[98] private communication with Mr. Mattenberger, laboratory of solid states physics, ETH Zürich

[99] HTS wire information for ETH Zürich via email
Garry Ferguson, AMSC HTS Account Rep